Summer 8-2016

Evaluation of Various Turbulence Models for Shock-Wave Boundary Layer Interaction Flows

Francis K. Acquaye
Washington University in St Louis

WASHINGON UNIVERSITY IN ST. LOUIS

School of Engineering and Applied Science

Department of Mechanical Engineering and Material Science

Thesis Examination Committee:

Dr. Ramesh K. Agarwal (Chair)

Dr. David A. Peters

Dr. Kenneth Jerina

Evaluation of Various Turbulence Models for Shock-Wave Boundary Layer Interaction Flows

by

Francis Kofi Acquaye

A thesis presented to the School of Engineering and Applied Science

of Washington University in partial fulfillment of the

requirements for the degree of

Master of Science

August 2016

Saint Louis, Missouri

Table of Contents

List of Figures

List of Tables

Acknowledgements

I would like to thank Dr. Ramesh K. Agarwal for taking me under his wing and for all his encouragement and guidance in my work. He has been an invaluable mentor and I am thankful for all the time and instruction he has given me. Secondly, I would like to thank Timothy Wray for answering all of my questions, no matter how trivial, without whom my research would not have been successful.

Lastly, but certainly not least, I want to thank my parents and family who have never wavered in their love and support of me and my academic pursuits. All great things that I have accomplished, I owe to them.

Francis Kofi Acquaye

Washington University in St. Louis

August 2016

ABSTRACT OF THE THESIS

Evaluation of Various Turbulence Models for Shock-Wave Boundary Layer Interaction Flows

By

Francis Kofi Acquaye

Department of Mechanical Engineering and Materials Science

Washington University in St Louis, 2016

Research Advisor: Dr. Ramesh K. Agarwal

Abstract

Despite the modeling capabilities of current computational fluid dynamics (CFD), there still exist problems and inconsistencies in simulating fluid flow in certain flow regimes. Most difficult are the high-speed transonic, supersonic and hypersonic wall-bounded turbulent flows with small or massive regions of separation. To address the problem of the lack of computational accuracy in turbulence modeling, NASA has established the Turbulence Modeling Resource (TMR) website and has issued the NASA 40% Challenge. The aim of this challenge is to identify and improve/develop turbulence and transition models as well as numerical techniques to achieve a 40% reduction in the predictive error in computation of benchmark test cases for turbulent flows. One of the phenomena of considerable interest in the 40% Challenge is the shock-wave boundary layer interaction (SWBLI) that occurs on aircraft surfaces at transonic and supersonic speeds and on space vehicles at hypersonic speeds. The correct modeling of shock-waves is complex enough, but the occurrence of SWBLI adds to the complexity by promoting flow separation, heat transfer,

and pressure gradients on the surface. SWBLI may occur in both the external and internal flow path of air and space vehicles; therefore, it is important to accurately predict this phenomenon to improve the design of aircraft and space vehicles.

The majority of CFD codes utilize the Reynolds Averaged Navier-Stokes (RANS) equations and employ various turbulence models. The most common among these turbulent models are the one-equation Spalart-Allmaras (SA) model and the two-equation Shear Stress Transport (SST) k-ω model. In recent years the CFD community has, in greater number, also started to adopt Large-Eddy Simulation (LES), Direct Numerical Simulation (DNS), and hybrid RANS-LES approaches for improving the accuracy of simulations. However currently, solving the RANS equations with eddy-viscosity turbulence models remains the most commonly used simulation technique in industrial applications. In this research, the one-equation Wray-Agarwal (WA), SA, and SST k-ω turbulence models are used to simulate supersonic flows in a 2D compression corner at angles of 8° and 16°, a partial axisymmetric flare of 20°, a full-body conical axisymmetric flare of 20°, and an impinging shock over a flat plate at 6°, 10°, and 14°. The ANSYS Fluent and OpenFOAM flow solvers are employed. Inflow boundary conditions and mesh sensitivity are examined to ensure the grid independence of computed solutions. For each of the three turbulence models, heat transfer, surface pressure, skin friction, and velocity profiles are compared with the available experimental data. It is found that the results from the WA model are in similar or better agreement with the experimental data compared to the SA and SST k-ω models for the majority of cases considered.

Chapter 1

Introduction

1.1 Development of Computational Fluid Dynamics and its Capabilities

In 1759, Leonhard Euler published his equations of motion for a fluid. A major triumph in predicting fluid flow, these equations expressed fluid dynamics in the form of partial differential equations. The Euler equations failed, however, to include friction forces experienced by the fluid. It was in 1845 that George Stokes developed more advanced equations describing the motion of viscous fluids [1]. The equations that Stokes derived had already existed since 1822, albeit for incompressible fluids; they were introduced by Claude Navier. Because of their complexity and highly nonlinear nature, many simplifications to the equations were required to obtain an analytic solution. The few analytical solutions that could be obtained nevertheless provided useful insight into viscous fluid behavior in simple geometries. Analytical methods could not, however, be applied to obtain complete explicit solutions to flows past or in complex geometries [2]. Since their introduction, the Navier-Stokes equations have been instrumental in fluid dynamics for understanding and analyzing the behavior of continuum fluid motion.

Because of their nonlinearity, only recently since the 1980s has it become possible to solve the Navier-Stokes equations numerically using a computer. With the continuous increase in computer power in the past several decades, it is now becoming possible to solve the steady/unsteady Navier-Stokes equations for computations of turbulent flows in and around the complex 3D geometries

encountered in industrial applications. This development has given rise to the field of Computational Fluid Dynamics (CFD).

To make the numerical simulation possible, new algorithms had to be developed. These algorithms are numerical procedures required to solve the Navier-Stokes equations, and since the advent of parallel and supercomputing, special algorithms have been created. The application of CFD is constantly expanding with the growth in computational power that can be effectively parallelized, as well as in the affordability of computational resources. CFD can also provide detailed information about a flow problem relatively quickly with less cost compared to experimental techniques. Despite this, CFD cannot fully replace experimental measurements outright, primarily because of the difficulty in modeling unsteady turbulent flows. Instead, CFD can substantially reduce the amount of experimental testing required and thus the overall cost [3]. In addition, the accuracy of a CFD simulation is dependent upon:

1. The accuracy of the mathematical model employed; e.g. it becomes difficult to model complex multi-physics flows with chemical reactions
2. The accuracy of the numerical solution machinery; e.g. the mesh, numerical algorithm, and boundary conditions

Figure 1.1 shows a typical CFD solution for a flow past a space shuttle with boosters.

Figure 1.1: Example of CFD application [4]

Despite the modeling capabilities of CFD, there still exist problems and inconsistencies in simulating certain flow regimes. For example, the reliability of CFD simulations is currently greater:

1. For laminar and incompressible attached turbulent flows than high-speed flows with separation
2. For single-phase flows than for multi-phase flows
3. For chemically inert flows than for reactive flows

Most difficult among these is the modeling of separated turbulent flows. To address the problem of computational accuracy in turbulence modeling, NASA has established the Turbulence Modeling Resource (TMR) website and issued the NASA 40% Challenge. The aim of the challenge is to identify and demonstrate simulation technologies that can reduce the predictive error of standard test cases for turbulent flow by 40% by 2025 [5]. Overseeing this endeavor is the Turbulence Models Benchmarking Working Group (TMBWG), a working group of the Fluid

Dynamics Technical Committee of the American Institute of Aeronautics and Astronautics (AIAA).

1.2 Shock-Wave Boundary Layer Interactions and their Significance

A phenomenon of prime concern in NASA's 40% Challenge is that of shock-wave boundary layer interactions (SWBLI) that arise on the surface of aircraft and space vehicles travelling at supersonic and hypersonic speeds. The correct modeling of shock-waves is complex enough, but the occurrence of SWBLIs results in flow separation, heat transfer, and pressure gradients. Furthermore, the shock-wave boundary layer interaction can also lead to an increase in flow unsteadiness. SWBLIs arise in both the external and internal flowpath of transonic, supersonic, and hypersonic air and space vehicles; therefore, it is important to accurately predict this phenomenon to improve the performance and design of high-speed aerospace vehicles.

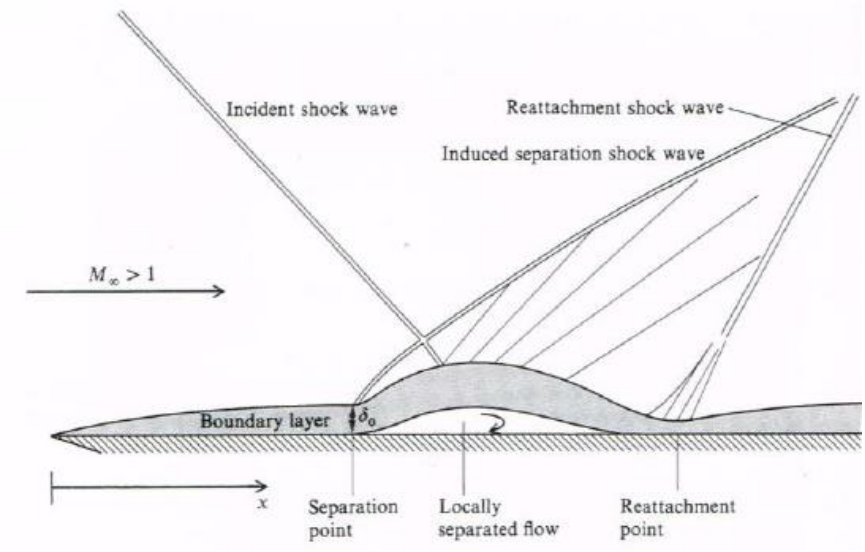

Figure 1.2: Schematic of shock-wave boundary layer interaction [4]

Figure 1.2 shows the schematic of a shock-wave boundary layer interaction on a flat plate. Figure 1.3 shows the conceptual artist rendering of a supersonic Boeing X-51; this vehicle experiences SWBLIs in certain segments of its flight regime.

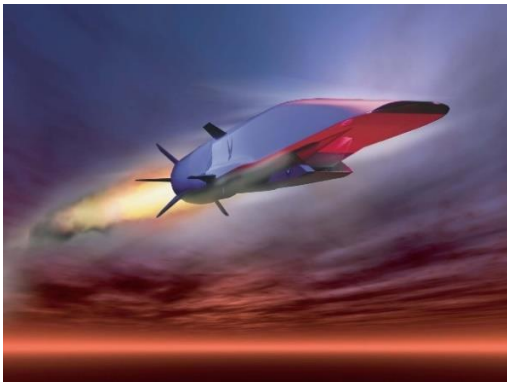

Figure 1.3: Artist's rendering of the hypersonic Boeing X-51 [6]

1.3 Review of Literature

The investigation of shock-wave boundary layer interactions has been a topic of interest in the aerospace community since Ferri's first observations of the phenomenon in 1939 [7]. In the mid-1940s, further research by Fage and Sargent, Ackeret et al., and Donaldson [8] demonstrated the importance of SWBLIs in transonic flight [9]. These investigations and a series of experiments performed in the late 1940s and early 1950s provided data and detailed visualizations showing the effects of Reynolds number, Mach number, and shock strength on SWBLIs. In a review article, Dolling [9] mentions that much of the work on SWBLIs until 1955 has been summarized by Holder et al. [10]. For the validation of theoretical and computational models, two-dimensional SWBLIs have been more widely studied then three-dimensional interactions. This is in part due to the relatively simple nature of two-dimensional interactions, but also due to a lack of information

available in the literature for three-dimensional interactions [11]. Among the two-dimensional validation cases, a SWBLI in a compression corner is one of the simplest configurations. A great deal of the experimental data for the case has been provided by Settles [12] and others. Shock-wave boundary layer interactions produced by an impinging/reflected shock on a flat plate is another test case that has been extensively studied for CFD validation. SWBLI cases using axisymmetric geometries are more complex than two-dimensional cases but are useful in providing important information for space vehicles which tend to be largely axisymmetric. Settles and Dodson searched through more than 105 data sets to find test cases for investigating SWBLIs for the validation of computer codes [11]. They identified numerous experiments and validation studies from 1972 to 1993, including two-dimensional incident shock-waves and axisymmetric geometries. Since many of these studies contained errors, inadequate data sets, or a lack of information, only a handful of the experiments and computer validations were deemed acceptable by Settles and Dodson. The last decade has seen renewed efforts to obtain more experimental data on SWBLIs.

Due to the NASA 40% Challenge for improving the prediction of CFD simulations, current research involves improving the prediction of shock-wave boundary layer interactions using a number of turbulence models. This includes several variants of the Spalart-Allmaras and Shear Stress Transport k-ω turbulence models. This thesis focuses on the validation of the newly developed Wray-Agarwal turbulence model for computation of shock-wave boundary layer interaction flows listed on NASA's TMR website.

Chapter 2

Turbulence Modeling

2.1 Turbulence Models

Behavior of laminar flow is determined by a single length scale, which mainly comes from the boundaries of the flow region. If one can accurately describe the boundaries of a laminar flow region, its flow behavior can be calculated precisely using the Navier-Stokes equations. For very simple geometries and fully developed flows, it has been possible to obtain exact analytical solutions. However, when the flow becomes turbulent, the fluctuations can only be fully characterized by an infinite number of length and time scales varying from very small to large values. It is now recognized that the simplest turbulent fluid behavior can be composed into large eddies and small eddies. Dating back to the early 1900s, since Osborne Reynolds, there have been three major approaches that have been developed to model and mathematically approximate turbulent fluid behavior. The oldest approach, developed in early 1900, is based on time-averaging of the Navier-Stokes equations, which results in the Reynolds-Averaged Navier-Stokes (RANS) equations. RANS averaging produces the so-called “turbulent stresses” or “Reynolds stresses,” which are unknown and requires modeling using empiricism. Thus RANS equations are not closed; this is known as the “Closure Problem” in RANS equations. Closure of the RANS equations requires empirical models for Reynolds stresses; these models are called the “turbulence models.” The solutions of RANS equations with turbulence models remains the most widely used method in industry for solving turbulent flows.

There are two other approaches that have developed since the 1980s which are more accurate than employing the RANS equations but are computationally very intensive and are still not practical for industrial applications. These are known as the Large Eddy Simulation (LES) and the Direct Numerical Simulation (DNS). The Sub-Grid Scale (SGS) model is used in LES to reduce the computational cost. In LES, the velocity field is filtered to separate the motion of large and small eddies. The large eddies are resolved directly without modeling, while the smaller eddies require modeling. The models used to characterize the small eddies are called the Sub-Grid Scale (SGS) models. The most well-known are the Smagorinsky model and Germano model, along with others. LES has a much higher level of accuracy compared to RANS but is computationally expensive, especially for computing turbulent boundary layers. In DNS, all the length scales, from the largest down to the Kolmogorov scale where the turbulent kinetic energy is dissipated to heat, have the turbulent flow resolved by solving the Navier-Stokes equations directly without any modeling. DNS is the most accurate method but has the highest computational cost and requires enormous computing power. Currently, DNS is affordable only for calculating flows at low Reynolds numbers with the simplest geometries.

As mentioned before, most of the industrial flows in complex 3D geometries are currently computed using the RANS equations with a turbulence model. In this thesis, RANS equations are solved in conjunction with a turbulence model using the commercial CFD code ANSYS Fluent. Two of the most widely used turbulence models, namely the one-equation Spalart-Allmaras (SA) and two-equation Shear Stress Transport (SST) k-ω models, and the recently developed one-equation Wray-Agarwal (WA) model are employed for computing the shock-wave turbulent boundary layer interaction flows. These three models are described briefly below.

2.1.1 Spalart-Allmaras Model

The Spalart-Allmaras (SA) turbulence model is the most common industry-used, one-equation, eddy-viscosity turbulence model. It was derived for application to aerodynamic flows using empiricism and arguments of dimensional analysis. The full formulation of the model is given by Spalart and Allmaras [13]. The transport equation for the modified turbulent viscosity $\tilde{\nu}$ is given by:

$$\frac{D\tilde{\nu}}{Dt} = c_{b1}[1 - f_{t2}]\,\tilde{S}\,\tilde{\nu} + \frac{1}{\sigma}\left[\nabla.\left((\nu + \tilde{\nu})\,\nabla\tilde{\nu}\right) + c_{b2}(\nabla\tilde{\nu})^2\right] - \left[c_{w1}f_w - \frac{c_{b1}}{\kappa^2}f_{t2}\right]\left[\frac{\tilde{\nu}}{d}\right]^2 \quad (1)$$

The turbulent eddy-viscosity is given by the equation:

$$\nu_t = \tilde{\nu}\, f_{v1} \quad (2)$$

Near wall blocking is accounted for by the damping function f_{v1}.

$$f_{v1} = \frac{\chi^3}{\chi^3 + c^3{}_{v1}}, \qquad \chi \equiv \frac{\tilde{\nu}}{\nu} \quad (3)$$

The remaining function definitions are given by the following equations:

$$\tilde{S} \equiv \Omega + \frac{\tilde{\nu}}{\kappa^2 d^2} f_{v2}, \qquad f_{v2} = 1 - \frac{\chi}{1 - \chi f_{v1}} \quad (4)$$

$$f_w = g\left[\frac{1 + c^6{}_{w3}}{g^6 + c^6{}_{w3}}\right]^{1/6}, \quad (5)$$

$$g = r + c_{w2}(r^6 - r), \quad (6)$$

$$r \equiv \frac{\tilde{\nu}}{\tilde{S}\,\kappa^2 d^2}, \quad (7)$$

$$f_{t2} = C_{t3} exp(-C_{t4}\chi^2) \quad (8)$$

2.1.2 Shear Stress Transport *k-ω* Model

The SST *k-ω* turbulence model, also widely used in the industry, is a two-equation, linear, eddy-viscosity model combining the best characteristics of the *k-ω* and *k-ε* turbulence models. Near solid boundaries, it behaves as a regular *k-ω* model directly integrable down to the wall, without the additional corrections seen in most *k-ε* models. In the free stream and shear layers, its behavior returns to a *k-ε* type model. This avoids the strong freestream sensitivity common to *k-ω* type models. The full formulation of the model is given by Menter [14]. The transport equations for *k* and *ω* are given by:

$$\frac{D\rho k}{Dt} = \tau_{ij}\frac{\partial u_i}{\partial x_j} - \beta^*\rho\omega\kappa + \frac{\partial}{\partial x_j}\left[(\mu + \sigma_k\mu_t)\frac{\partial k}{\partial x_j}\right] \tag{9}$$

$$\frac{D\rho\omega}{Dt} = \frac{\gamma}{\nu_t}\tau_{ij}\frac{\partial u_i}{\partial x_j} - \beta^*\rho\omega^2 + \frac{\partial}{\partial x_j}\left[(\mu + \sigma_\omega\mu_t)\frac{\partial \omega}{\partial x_j}\right] + 2(1-F_1)\rho\sigma_{\omega 2}\frac{1}{\omega}\frac{\partial k}{\partial x_j}\frac{\partial \omega}{\partial x_j} \tag{10}$$

The turbulent eddy-viscosity is computed from:

$$\nu_t = \frac{a_1 k}{\max(a_1\omega; \Omega F_2)}\,,\ \ \Omega = \sqrt{2W_{ij}W_{ij}}\,,\ \ W_{ij} = \frac{1}{2}\left(\frac{\partial u_i}{\partial x_j} - \frac{\partial u_j}{\partial x_i}\right) \tag{11}$$

Each model constant is blended between an inner and outer constant by:

$$\varphi_1 = F_1\varphi_1 + (1-F_1)\varphi_2 \tag{12}$$

The remaining function definitions are given by the following equations:

$$F_1 = tanh(arg_1^4) \tag{13}$$

$$arg_1 = \min\left[\max\left(\frac{\sqrt{k}}{\beta^*\omega d}, \frac{500\nu}{d^2\omega}\right), \frac{4\rho\sigma_{\omega 2}k}{CD_{k\omega}d^2}\right] \tag{14}$$

$$CD_k = \max\left(2\rho\sigma_{\omega 2}\frac{1}{\omega}\frac{\partial k}{\partial x_j}\frac{\partial \omega}{\partial x_j}, 10^{-20}\right) \tag{15}$$

$$F_2 = tanh(arg_2^2) \tag{16}$$

$$arg_2 = \max\left(2\frac{\sqrt{k}}{\beta^*\omega d}, \frac{500\nu}{d^2\omega}\right) \tag{17}$$

2.1.3 Wray-Agarwal Model

The Wray-Agarwal (WA) model is a recently developed, one-equation, eddy-viscosity model derived from *k*-ω closure. It has been applied to several canonical cases and has shown improved accuracy over the SA model and competitiveness with the SST *k*-ω model. An important distinction between the WA model and previous one-equation *k*-ω models is the inclusion of the cross diffusion term in the ω-equation and a blending function that eases the transition between the two destruction terms. The full formulation of the model is given by Menter in Ref. [14]. The undamped eddy-viscosity is determined by:

$$\frac{\partial R}{\partial t} + u_j \frac{\partial R}{\partial x_j} = \frac{\partial}{\partial x_j}\left[(\sigma_R R + \nu)\frac{\partial R}{\partial x_j}\right] + C_1 RS + f_1 C_{2k\omega}\frac{R}{S}\frac{\partial R}{\partial x_j}\frac{\partial S}{\partial x_j} - (1 - f_1)C_{2k\varepsilon}R^2\left(\frac{\frac{\partial S}{\partial x_j}\frac{\partial S}{\partial x_j}}{S^2}\right) \quad (18)$$

The turbulent eddy-viscosity is given by the equation:

$$\nu_T = f_\mu R \quad (19)$$

The wall blocking effect is accounted for by the damping function f_μ.

$$f_\mu = \frac{\chi^3}{\chi^3 + C_w^3}, \qquad \chi = \frac{R}{\nu} \quad (20)$$

Here *S* is the mean strain described below.

$$S = \sqrt{2S_{ij}S_{ij}}, \qquad S_{ij} = \frac{1}{2}\left(\frac{\partial u_i}{\partial x_j} + \frac{\partial u_j}{\partial x_i}\right) \quad (21)$$

While the $C_{2k\omega}$ term is active, Eq. (18) behaves as a one equation model based on the standard *k*-ω equations. The inclusion of the cross diffusion term in the derivation causes the additional $C_{2k\varepsilon}$ term to appear. This term corresponds to the destruction term of one-equation models derived from standard *k*-ε closure. The presence of both terms allows the new model to behave either as a one equation *k*-ω or one equation *k*-ε model based on the switching function f_1. The blending function

was designed so that the *k-ω* destruction term is active near solid boundaries while the *k-ε* destruction term becomes active near the end of the log-layer. The model constant C_b =1.66 controls the rate at which f_1 switches.

$$f_1 = tanh(arg_1^4) \tag{22}$$

$$arg_1 = \min\left(\frac{C_b R}{S\kappa^2 d^2}, \left(\frac{R+\nu}{\nu}\right)^2\right) \tag{23}$$

Chapter 3

Computational Tools

3.1 ANSYS Workbench

ANSYS Workbench is an integrated simulation platform which contains a number of integrated applications allowing multi-physics analyses and control of a simulation. It is based on a project's schematic view which ties together the entire simulation process using drag-and-drop modules [15]. Depending on the type of problem being examined, Workbench employs the necessary capabilities for the specific simulation task. The integrated applications pertinent to this thesis are ANSYS DesignModeler, ANSYS Meshing, ICEM and CFD-Post. The flow solver, ANSYS Fluent, can also be integrated into Workbench as desired.

3.1.1 ANSYS Fluent

ANSYS Fluent is a flow solver that solves the governing equations of fluid flow. It has many capabilities and numerical algorithms for solving the governing equations of inviscid, viscous, incompressible, compressible, laminar, and turbulent flows. It also supports a number of widely used turbulence models including the SA and SST k-ω models employed in this thesis for the solution of the RANS equations for turbulent flows.

As a first step in this research, the numerical solution procedure and implementations of the SA and SST k-ω models in Fluent were validated and verified by computing the flow for the 2D zero

pressure gradient, turbulent flat plate boundary layer flow. The flow conditions for this case are listed on the NASA TMR website [16]. The numerical results reported on the TMR website were performed using the NASA FUN3D code. The theory guide available for Fluent gives details on the SA and SST k-ω model implementations in Fluent [17]. The guide shows that additional modifications and limiters are present in both models in Fluent. To remedy this situation in order to compare the results with those given by the TMR, the SA-Standard and SST-V models were implemented in Fluent by use of User-Defined-Functions (UDF). Results of the baseline models in Fluent and modified models using UDF are shown in Figure 3.1 and Figure 3.2. Some discrepancy between the Fluent results and the FUN3D results remains. Since the magnitude of the error is comparable for both the SA and SST-V models, the error can likely be attributed to some numerical differences in the two codes or a post-processing error between the results. This inconsistency between the results is currently being investigated.

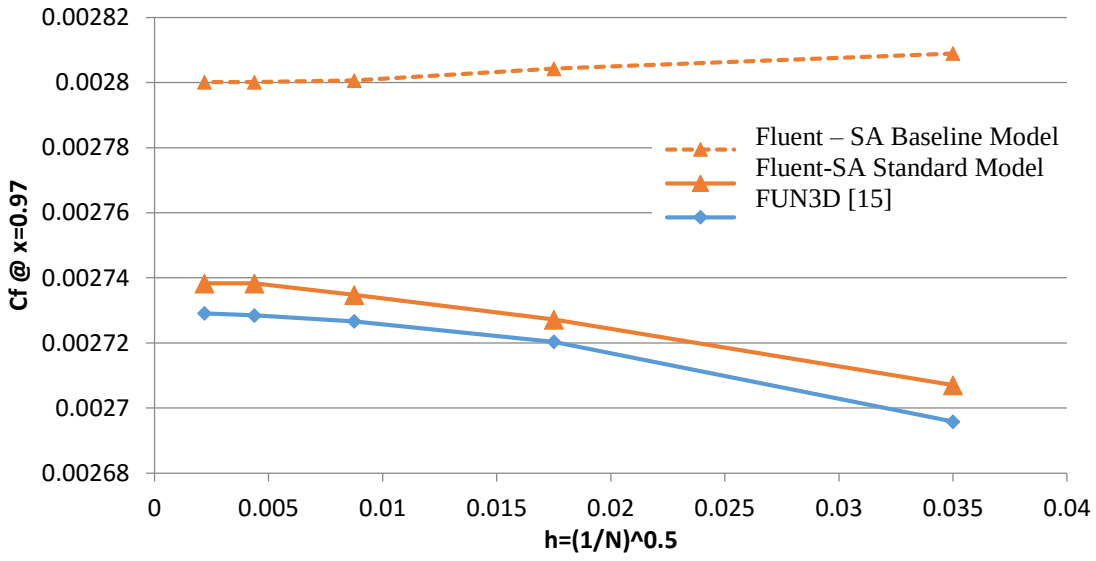

Figure 3.1: Verification and validation of Spalart-Allmaras Model in Fluent for 2D zero pressure gradient flat plate flow

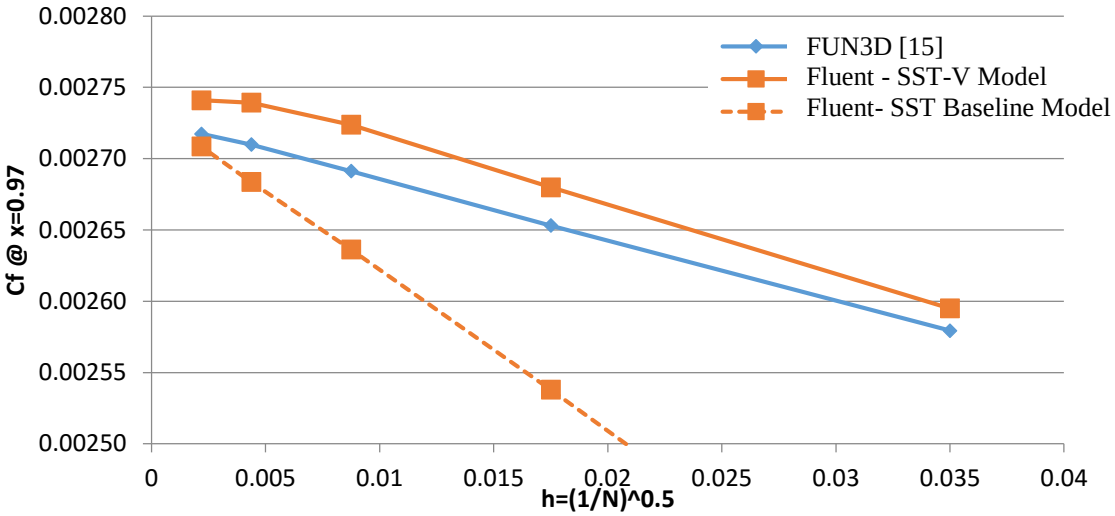

Figure 3.2: Verification and validation of SST *k-ω* model in Fluent for 2D zero pressure gradient flat plate flow

Chapter 4

Test Cases and Results

4.1 Flow Simulations Setup

ANSYS Workbench 16.1 and ANSYS Fluent 16.1 were installed on a PC in the CFD lab in the department of Mechanical Engineering and Material Science at Washington University in St. Louis. ANSYS Workbench and Fluent were run on a Dell OptiPlex 9020 PC with a quad core Intel i7-4790 CPU at 3.6 GHz, 16 GB of RAM, and a Windows 7 Professional 64-bit operating system.

The geometries of the cases were constructed using the Design Modeler application through ANSYS Workbench. Similarly, the meshes for the test cases were generated through the ANSYS Meshing and ICEM applications within ANSYS Workbench. Analysis of the results was completed through CFD-Post and Fluent.

After the successful completion of a run, a gradient adaption of the mesh is performed. This is done through Fluent and its purpose is to accurately and efficiently resolve all areas of the flow with high gradients.

Initially, a simulation run of a test case is conducted on a standard uniform or non-uniform mesh. The grid adaption algorithm in Fluent then automatically clusters the mesh in regions of high gradient in the flow, e.g., in regions of shock-waves and boundary layers/mixing layers. An example of a mesh before and after adaptive refinement is shown in Figure 4.1.

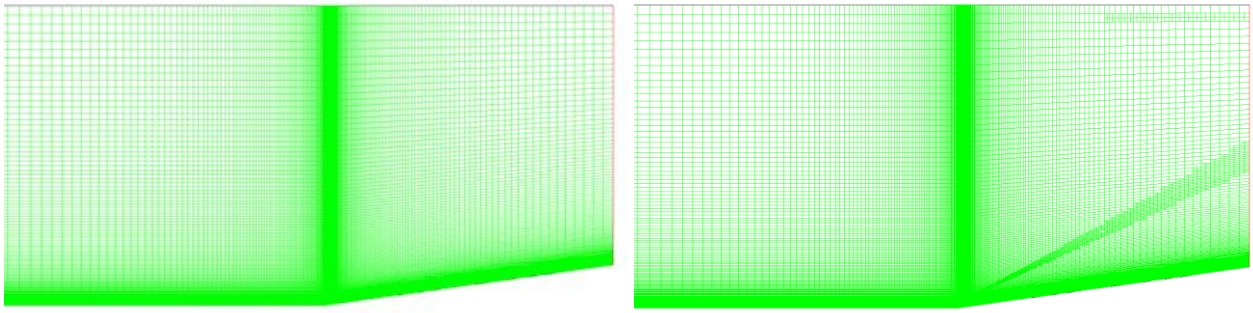

Figure 4.1: Example of original mesh (left), and same mesh after adaptive refinement (right). Note how additional cells are added in the region of a shock.

4.2 Supersonic Flow in a 2D Compression Corner

The supersonic flow past a 2D compression corner was simulated to give comparable results to the experiments of Settles et al. [12]. The data was taken from Settles' original publication along with revised data given by Settles and Dodson [18]. Additional data related to Settles' original experiment has been provided by Muck et al. [19], [20] . Figure 4.2 illustrates the setup for the 2D compression corner model.

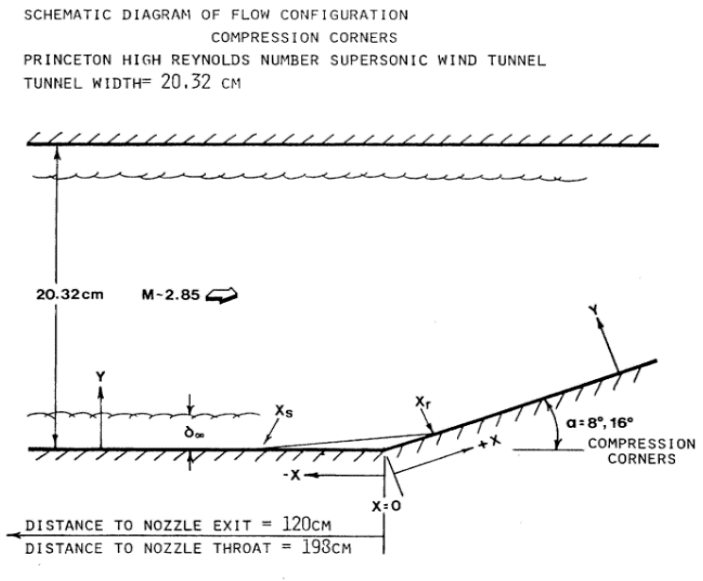

Figure 4.2: Schematic and dimensions of the flow setup for a 2D compression corner [12]

Both cases of the 8° and 16° compression corner angles are located at a distance of 1.205 m from the inlet boundary. The free stream is approximately at Mach 3. Freestream boundary conditions for the 8° and 16° corners are given below in Table 4.1. For this case, experimental quantities of wall pressure, skin friction coefficient, and velocity profiles are available. The computational grids used for the 8° and 16°compression corners are shown in Figure 4.3 and Figure 4.4, respectively.

Table 4.1: Freestream Boundary Conditions for 2D Compression Corner

Compression Corner	8°	16°
Mach Number	2.87	2.85
Static Temperature (Kelvin)	106	102
Wall Temperature (Kelvin)	291	282
Freestream Velocity (m/s)	592	576
Reynolds Number	6.3×10^7	6.3×10^7

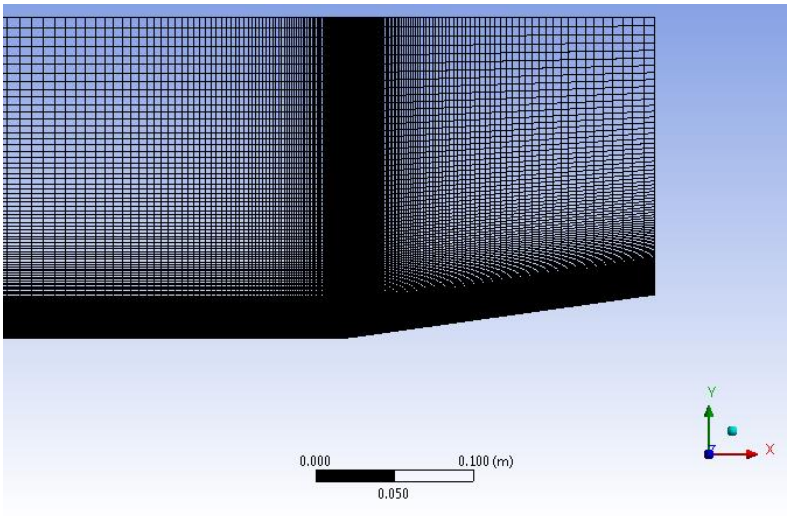

Figure 4.3: Mesh for 8° compression corner case

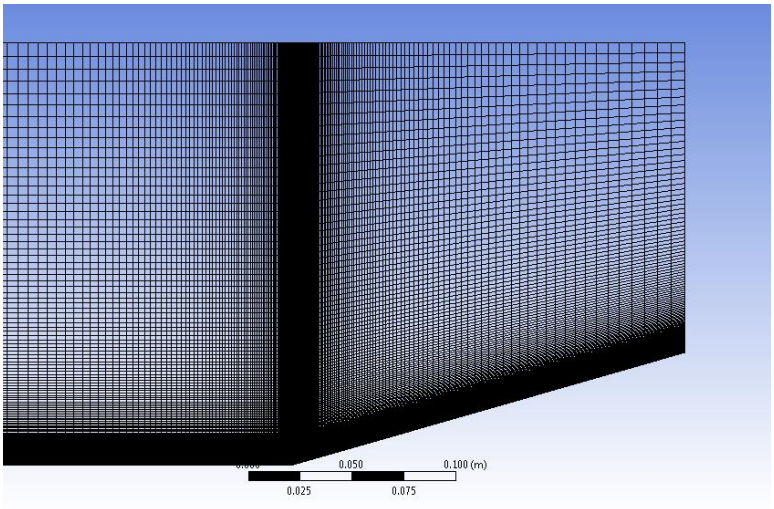

Figure 4.4: Mesh for 16° compression corner case

The original grid for both cases has 44800 elements with 45241 nodes. The mesh for each model was refined several times adapting to gradients of static pressure. The refinement information for both 8° and 16° compression corners is given below in Table 4.2.

Table 4.2: Mesh information for 8° and 16° compression corners for SA, SST *k-ω* and WA models

Angle	8°			16°		
Model	SA	SST	WA	SA	SST	WA
Nodes	164299	146090	174752	197199	203377	216357
Cells	162361	144324	172762	194998	200881	214075

Simulation results using the SA, SST *k-ω* and WA turbulence models are compared to the experimental data for both the 8° and 16° compression corners. For the 8° compression corner, pressure, skin friction and velocity profiles at various locations along the compression ramp are shown in Figure 4.5, Figure 4.6, and Figure 4.7, respectively. Examining the pressure predictions shown in Figure 4.5, it can be seen that all three turbulence models correctly predict the pressure leading up to the compression corner but overpredict the pressure downstream of the compression corner. The computations from all three turbulence models show little difference. A large difference, however, exists in the prediction of the skin friction coefficient shown in Figure 4.6. It can be seen that the SA and SST *k-ω* models predict a very small region of separation not seen in the experiment. While not correctly predicting the separation region, the WA model predicts a large peak not seen in the experiment. The cause of this peak is not clear and is currently under investigation.

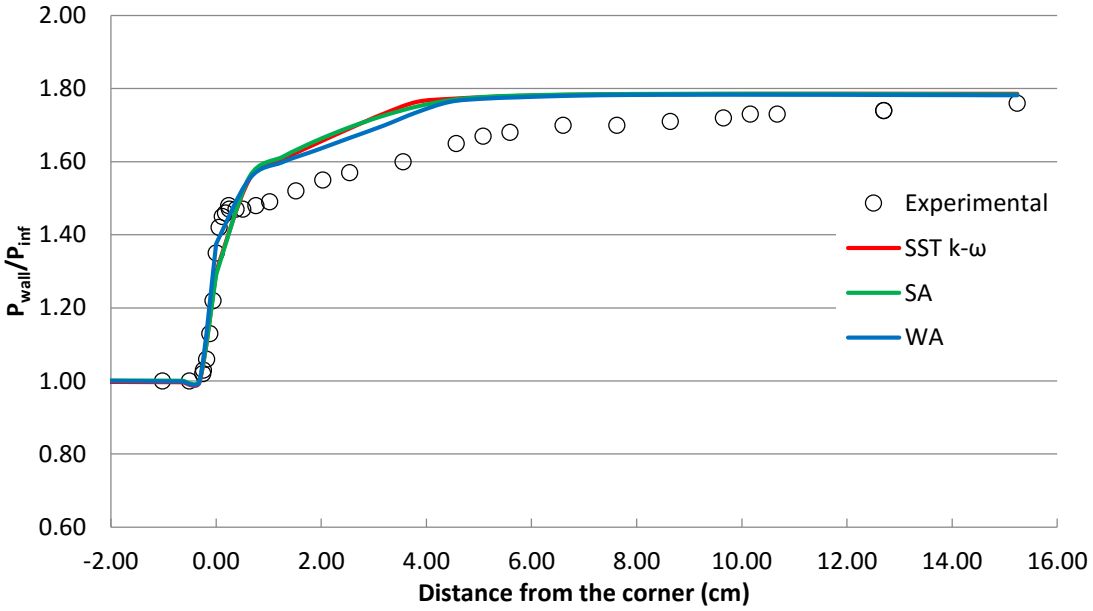

Figure 4.5: P_{wall}/P_{inf} vs. x (cm) for 8° compression corner

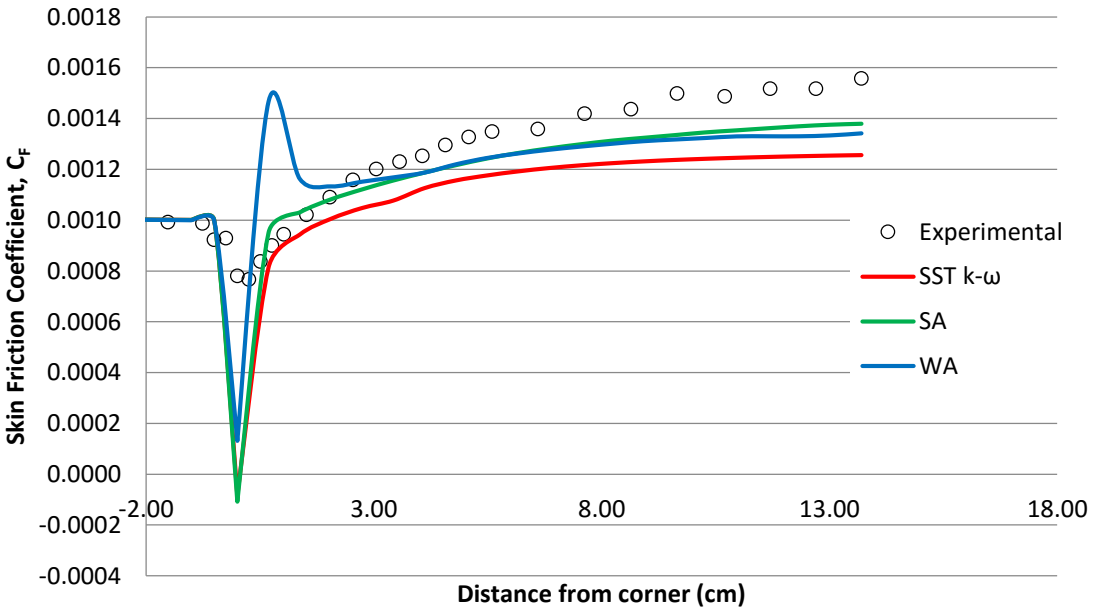

Figure 4.6: Skin friction coefficient vs. x (cm) for 8° compression corner

From Figure 4.7(a) and Figure 4.7(b) it can be seen that at locations before the compression corner, the WA model performs the best in predicting results similar to the experiment. At a location closely following the compression corner, illustrated in Figure 4.7(c), the SA and SST k-ω models give results that closely match the experimental data. The WA model predicts the general trend of the experimental velocity profiles but at slightly lower velocities near the wall. Further away from the compression corner, as shown in Figure 4.7(d), the SA and SST k-ω models give nearly identical results in predicting the velocity profiles. They are in good agreement with the experimental data. The WA model does only a slightly better job in predicting this velocity profile when compared to the experiment. Contour plots of Mach number for each of the turbulence models are shown in Figure 4.8.

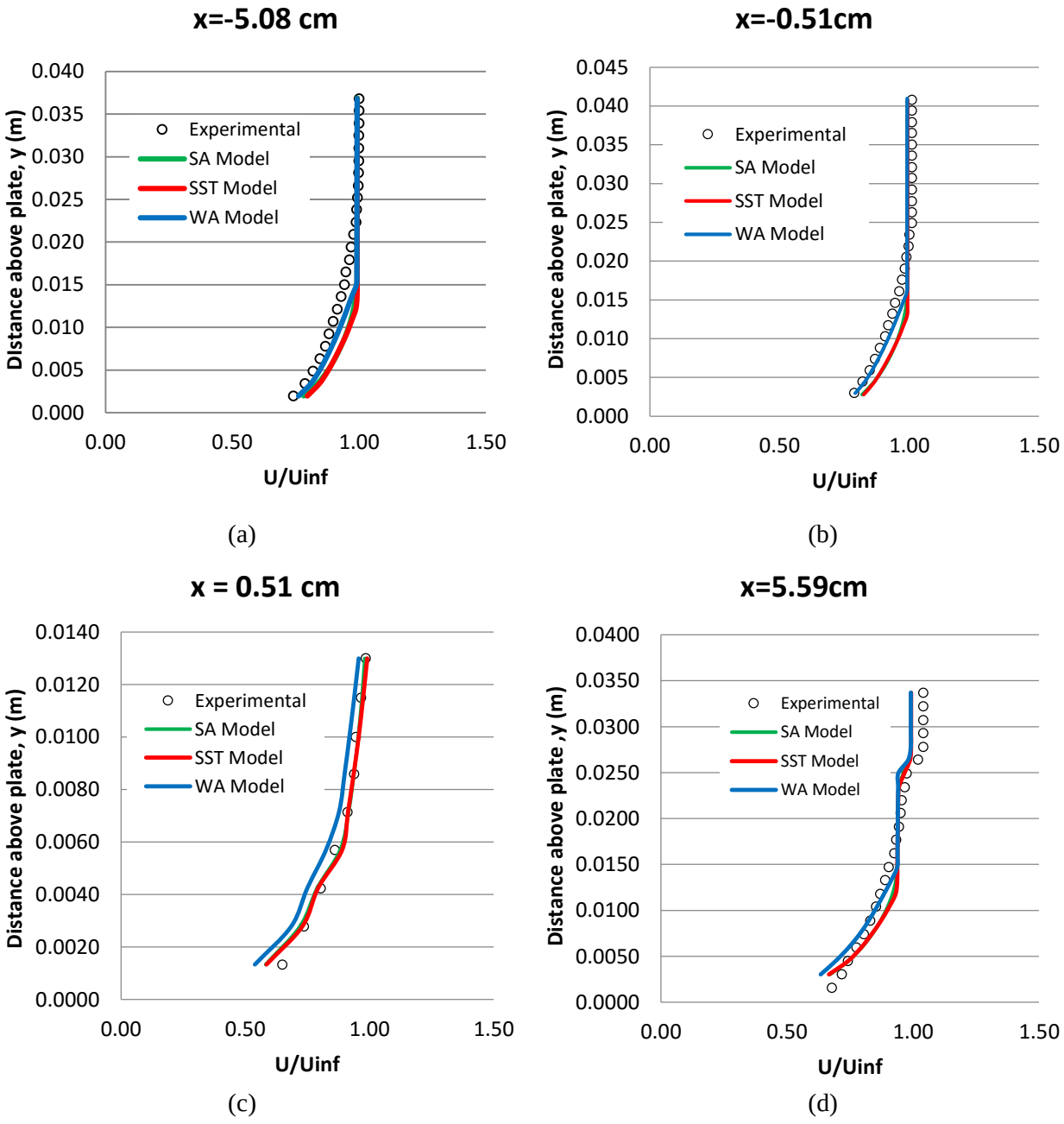

Figure 4.7: y (m) vs U/U_{inf} for 8° compression corner at locations (a) -5.08 cm, (b) -0.51 cm, (c) 0.51 cm, and (d) 5.59 cm from the compression corner (x = 0 is at the corner)

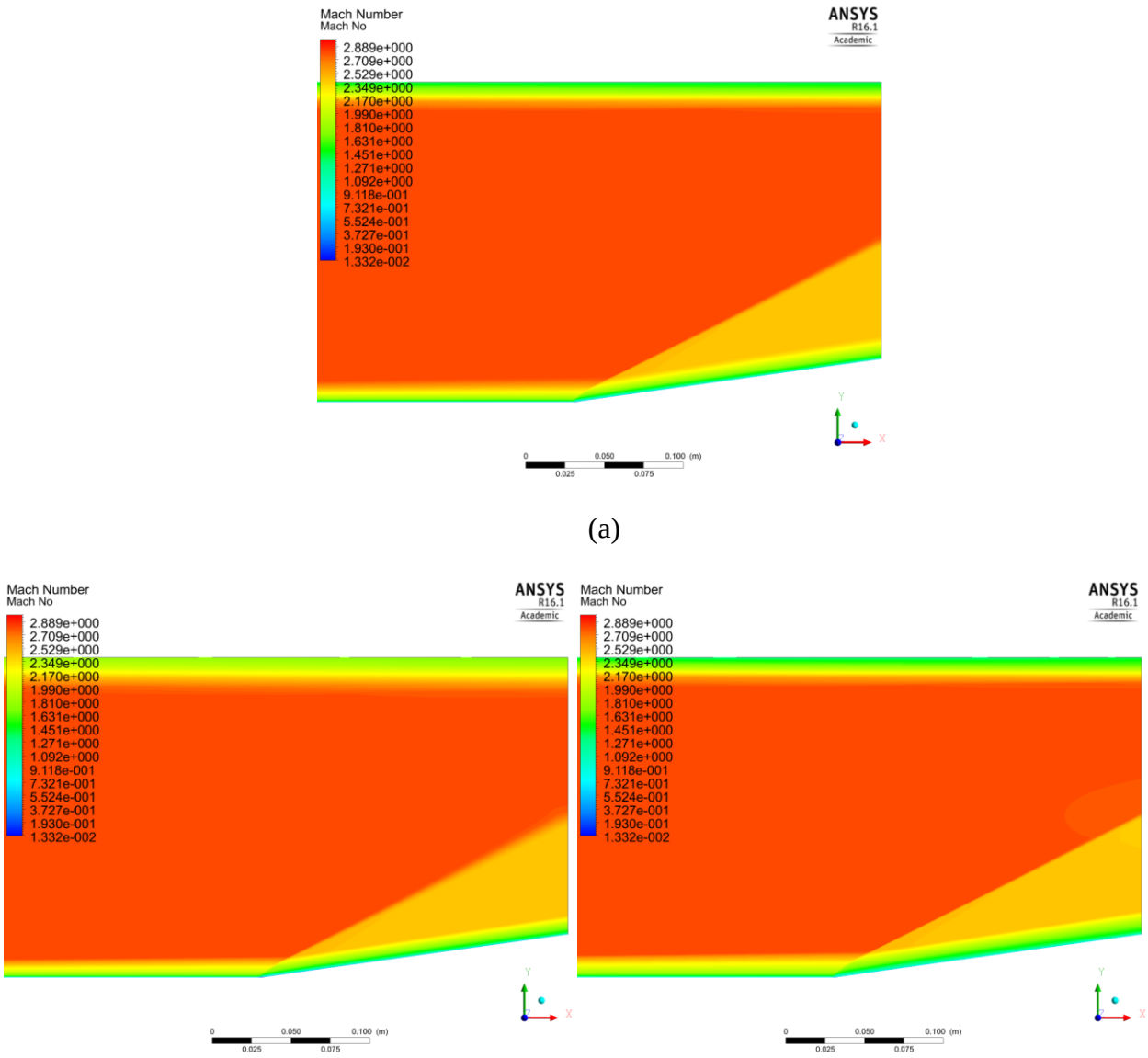

Figure 4.8: Mach Number contours for 8° compression corner of the (a) SA model, (b) SST model and (c) WA model

Simulation results for the 16° compression corner are shown in Figure 4.9, Figure 4.10, and Figure 4.11. Examining the normalized wall pressure versus distance along the compression corner in Figure 4.9, it can be seen that the WA and SA model do a better job at predicting the pressure leading up to the compression corner than the SST *k-ω* model. Away from the corner, all three

turbulence models follow the experimental data but differ in predicting the surface pressure close to and after the corner. The SST *k-ω* turbulence model shows a sudden increase in the surface pressure ahead of the compression corner in contrast to the results from the SA and WA models. This behavior is the result of the SST *k-ω* model predicting flow separation in the corner region. The adverse pressure gradient caused by the separated flow pushes the shock-wave upstream of the compression corner, which causes the SST *k-ω* model to predict the surface pressure at higher values earlier than the experimental data. The WA and SA models, however, do not predict large flow separation, and due to the presence of only a small region of separated flow in the experiment, the two models are closer to the experimental pressure than that predicted by the SST *k-ω* model. After the compression corner, however, the SA and WA models overpredict the surface pressure whereas the SST k-*ω* model is closer to the experimental data.

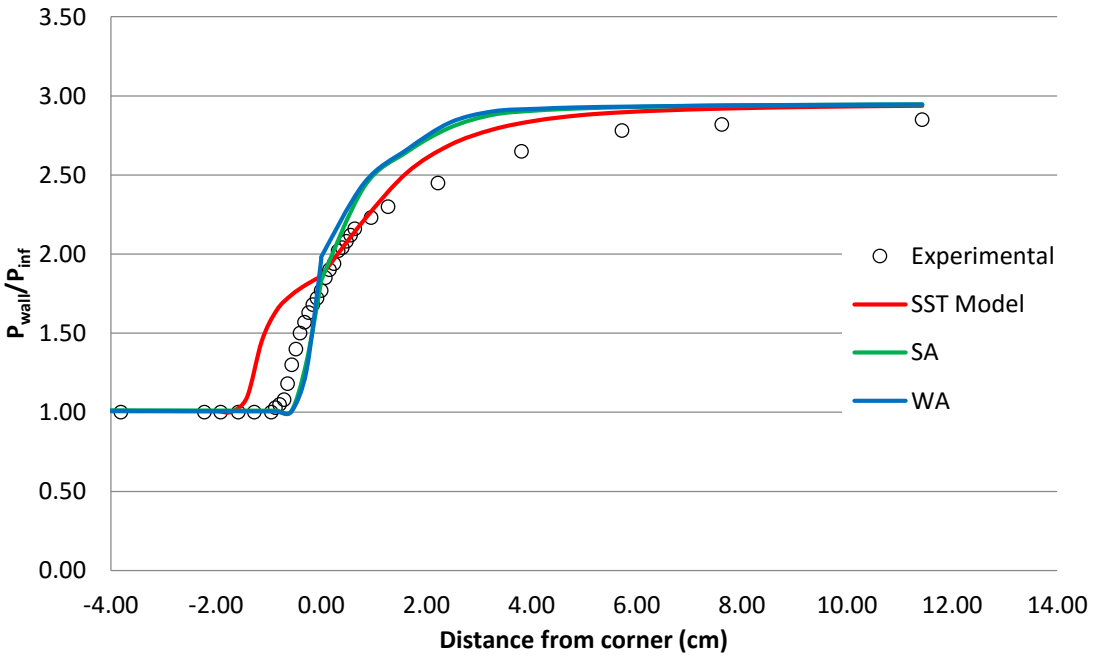

Figure 4.9: P_{wall}/P_{inf} vs. x (cm) for 16° compression corner

The plot of the skin friction coefficient versus distance along the 16° compression corner in Figure 4.10 further reinforces that the SST *k-ω* model predicts a large region of separated flow in the corner region. Not evident in the surface pressure plot, the WA model predicts a small region of separated flow while the SA model predicts no flow separation. However, a large peak after the compression corner is again present in the prediction of skin friction from the WA model. After the compression corner, the WA model follows the experimental data closely and is much more accurate than the SST *k-ω* and SA models. Far away from and downstream of the corner all three models tend to diverge away from the experimental data.

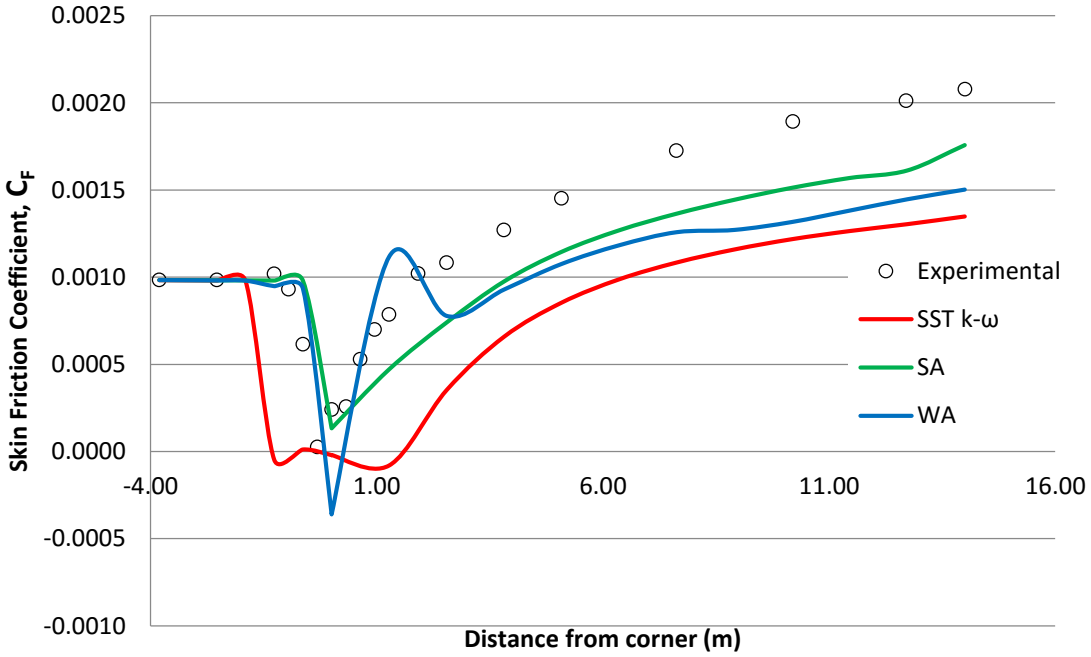

Figure 4.10: Skin friction coefficient vs. x (cm) for 16° compression corner

Figure 4.11 shows the velocity profiles at four locations along the bottom plate of the model. In a manner similar to the 8° compression corner case, the WA model performs the best in predicting the velocity profiles before the compression corner. After the compression corner, all three models adequately predict trends similar to the experimental data, but not one of the model's results match

the data satisfactorily. Contour plots of Mach number for each of the turbulence models are shown in Figure 4.9.

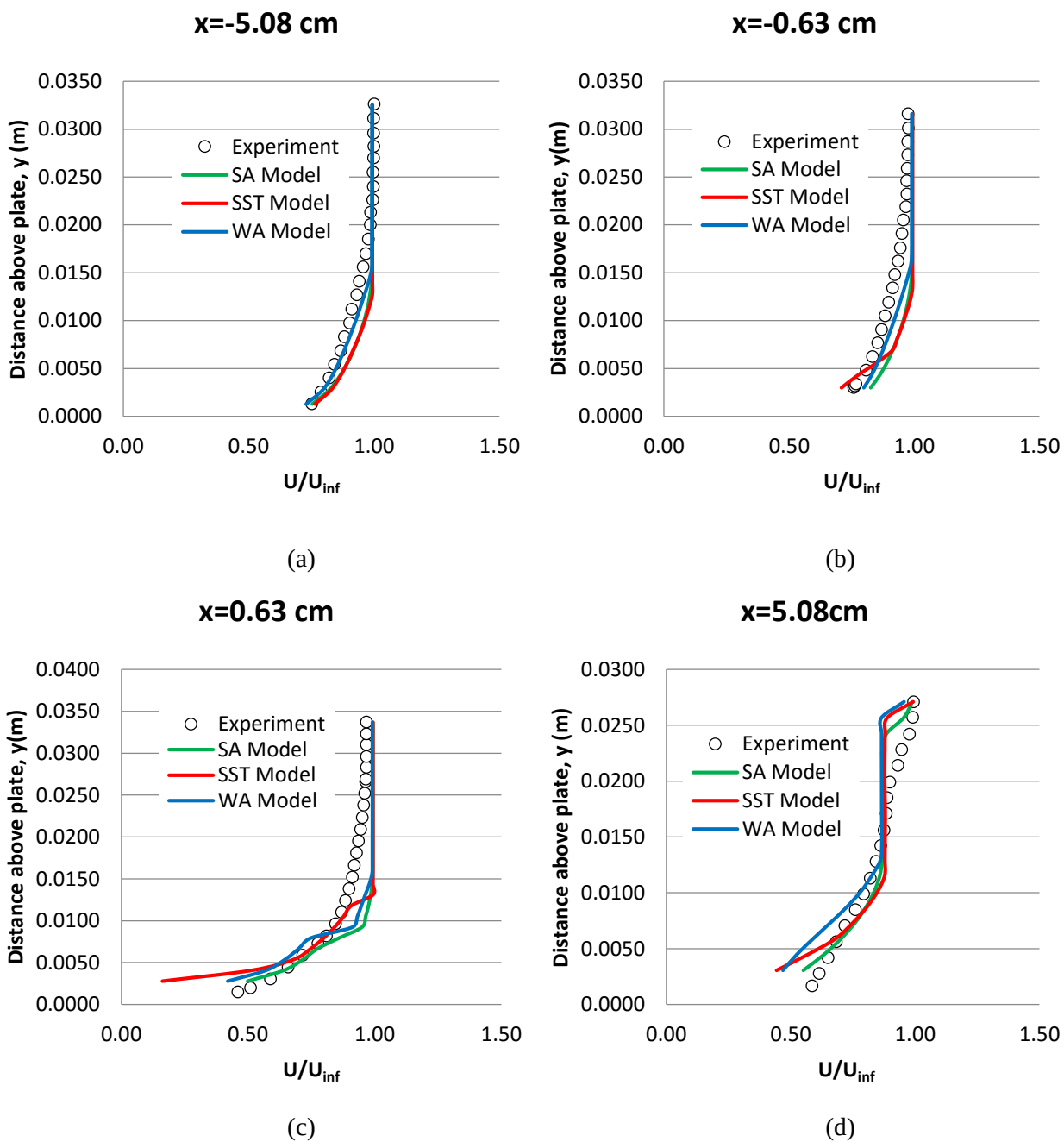

Figure 4.11: y (m) vs U/U_{inf} for 16° compression corner at locations (a) -5.08 cm, (b) -0.63 cm, (c) 0.63 cm, and (d) 5.08 cm from the compression corner (x = 0 is the location of the corner)

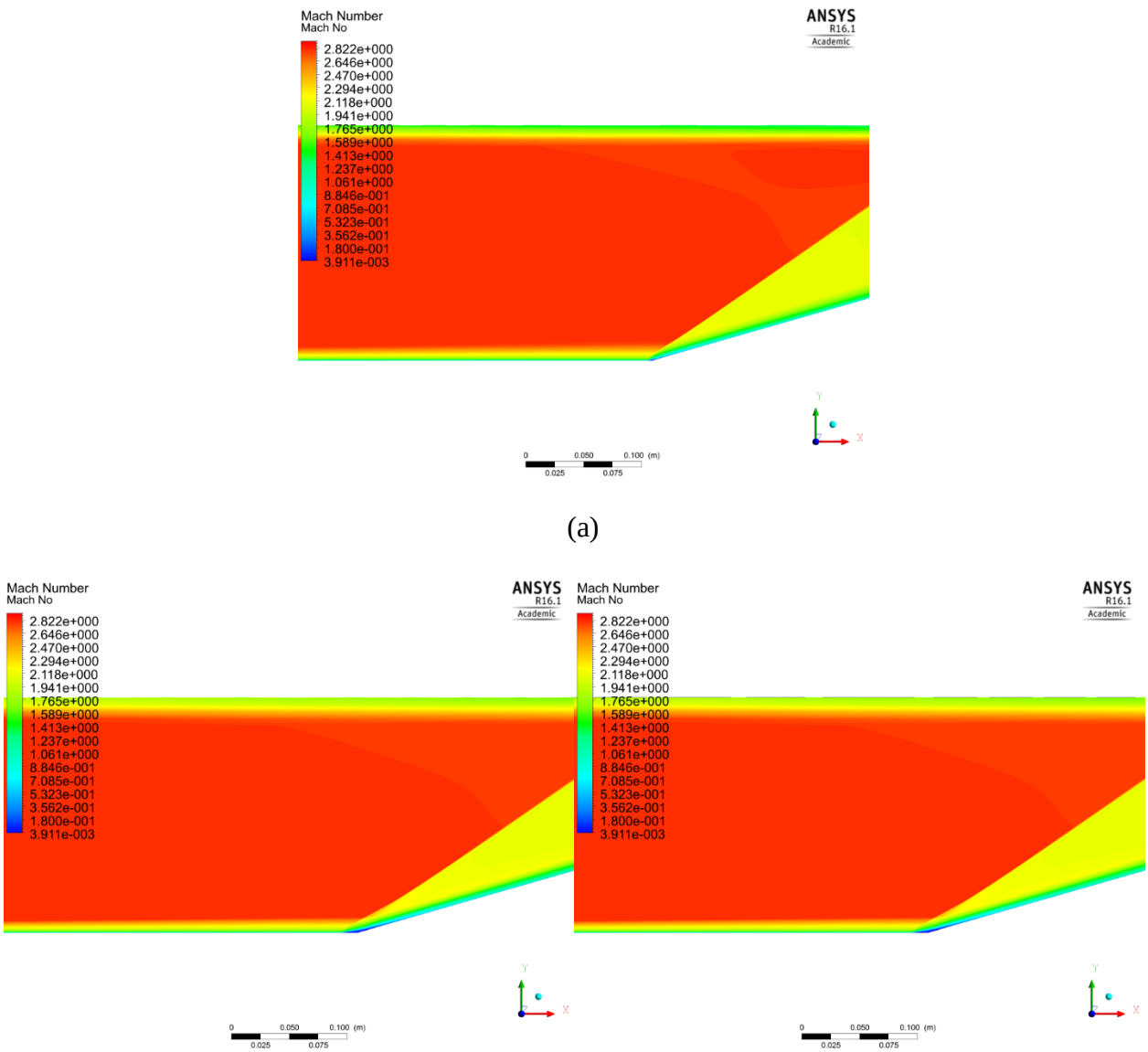

Figure 4.12: Mach number contours for 16° compression corner of the (a) SA model, (b) SST model and (c) WA model

4.3 Supersonic Flow past a Partial Axisymmetric Flare

This case involves a cone/ogive cylinder with flare of 20°. The experiments for this case have been performed by Kussoy and Horstman [21]. This case has also been identified as a NASA validation test case for turbulence models; both SA and SST *k-ω* models have predicted this case quite well as documented on the NASA Turbulence Modeling Resource (TMR) website [16]. This is therefore a good example to evaluate the WA model's performance. Additionally, the earlier computations of Georgiadis et al. [22] not only provide results via the NASA TMR, but the meshes are also available from the TMR for use for other investigators. The NASA results were computed using the Wind-US CFD solver. The freestream conditions are: $M_{ref} = 7.11, T_{ref} = 80\ K$, $Re_{ref} = 57060$, and $T_{wall} = 311K$. The computational grid is shown in Figure 4.13.

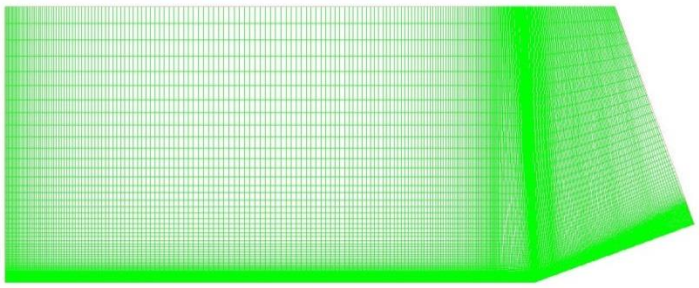

Figure 4.13: Initial mesh for partial axisymmetric flare of 20°

The mesh for the partial axisymmetric flare has 64000 cells and 64521 nodes. It was refined several times by applying adaptions to gradients of static pressure and total surface heat flux. The mesh is given in Table 4.3.

Table 4.3: Mesh information for partial axisymmetric flare for SA, SST *k-ω* and WA model

Angle	20°		
Model	SA	SST	WA
Nodes	71314	70936	76233
Cells	70003	69589	74338

Figure 15 compares the predicted surface pressure using various turbulence models with the experimental data. Comparing the WIND and Fluent results, it can be seen that the SST *k-ω* results from the two codes differ only slightly. The SA predictions show some difference from the experimental data at a distance of x ~ 3 cm from the flare. The cause of this difference requires further investigation. The WA model is in better agreement with the experimental data compared to all other models from a distance of x ~ 2 to 7 cm from the corner. After x = 7 cm, the results from all models are essentially the same.

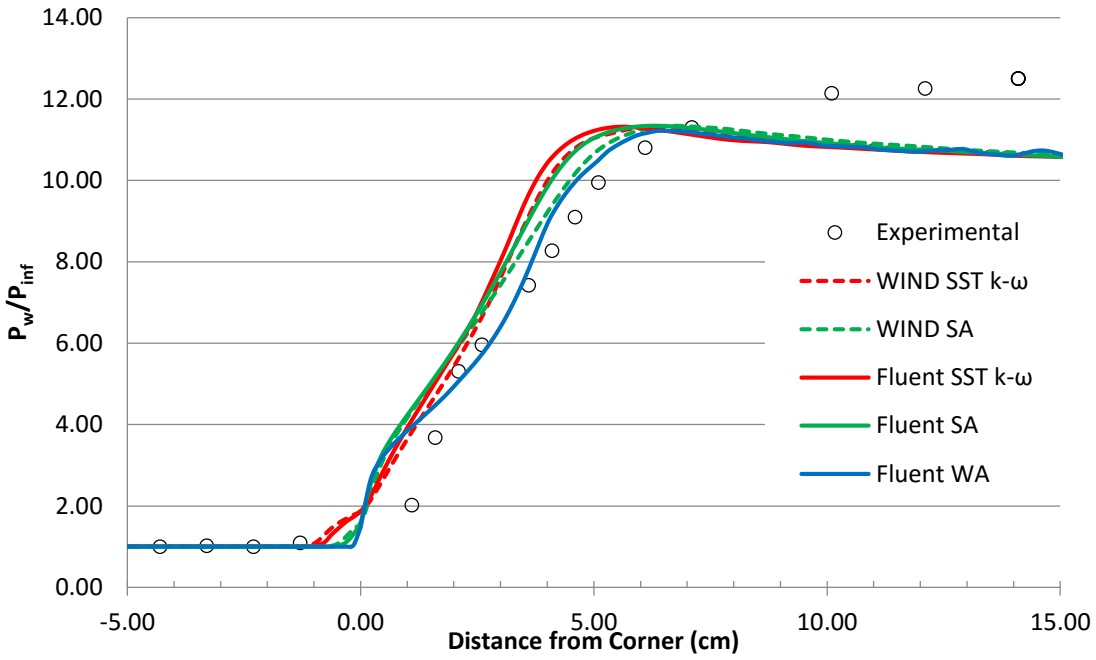

Figure 4.14: P_{wall}/P_{inf} vs. distance from corner (cm)

Examining the variation in wall heat transfer with distance from the flare, in Figure 4.15, the WIND and Fluent SST *k-ω* results are very similar until x ~ 5 cm, where the WIND results follow the experimental results just a bit closer. Again, between the WIND and Fluent SA model results, little distinction can be made until x ~ 3 cm, where the WIND results follow the experimental data more closely. Both the WIND and Fluent SA models give results that are closer to the experimental data than the results of the WIND and Fluent SST *k-ω* results. The WA model does well in predicting results closer to the experimental data. Furthermore, both the SA and SST *k-ω* models fail to predict the first heat transfer data point after the flare, whereas the WA model predicts it precisely but overestimates the wall heat transfer from x ~ 1 to 5 cm. After x ~ 5 cm, the WA model joins the WIND SST *k-ω* and SA models and the Fluent SA model in accuracy.

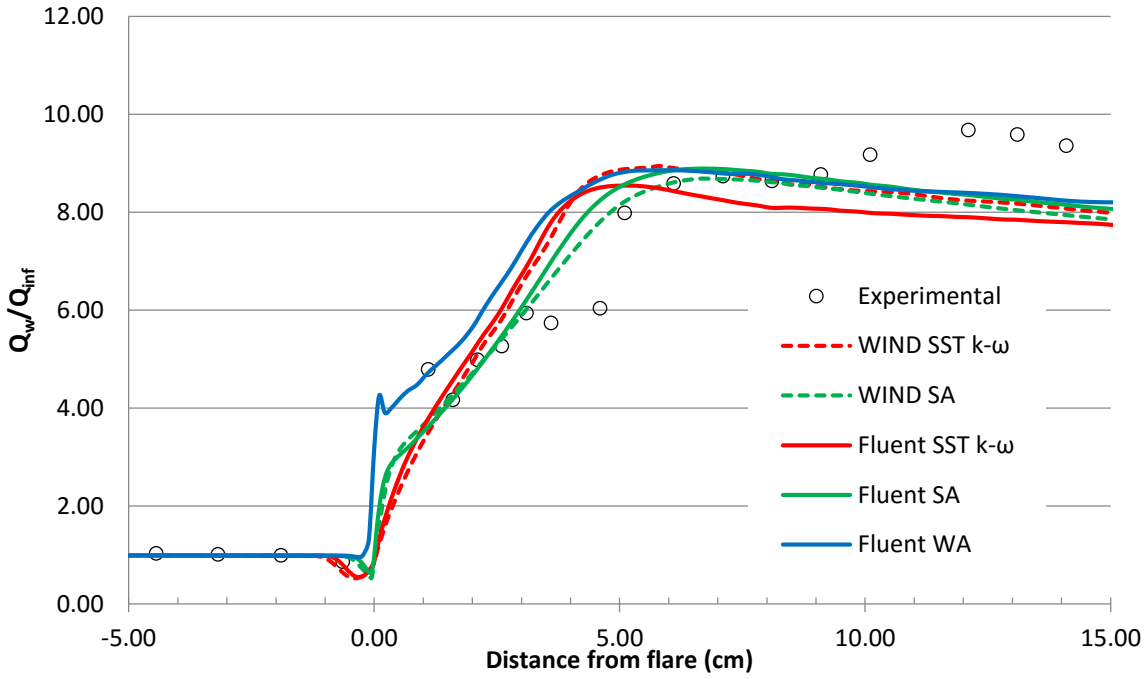

Figure 4.15: Q_{wall}/Q_{inf} vs. distance from flare (cm) for partial axisymmetric 20° flare

Figure 4.16 shows the results of the turbulence models for the velocity profile at x = 6 cm upstream of the flare. Comparing the WIND and Fluent results for the SST *k-ω* and SA turbulence models, no notable difference is observed and the models' results follow the experimental results quite well. The turbulence models predict a boundary layer very similar to the one developed in the experiment. Despite following the trend of the experiment, the WA model predicts a velocity profile that deviates noticeably from that obtained from other turbulent models and the experimental data. The reason for this unexpected result is being investigated.

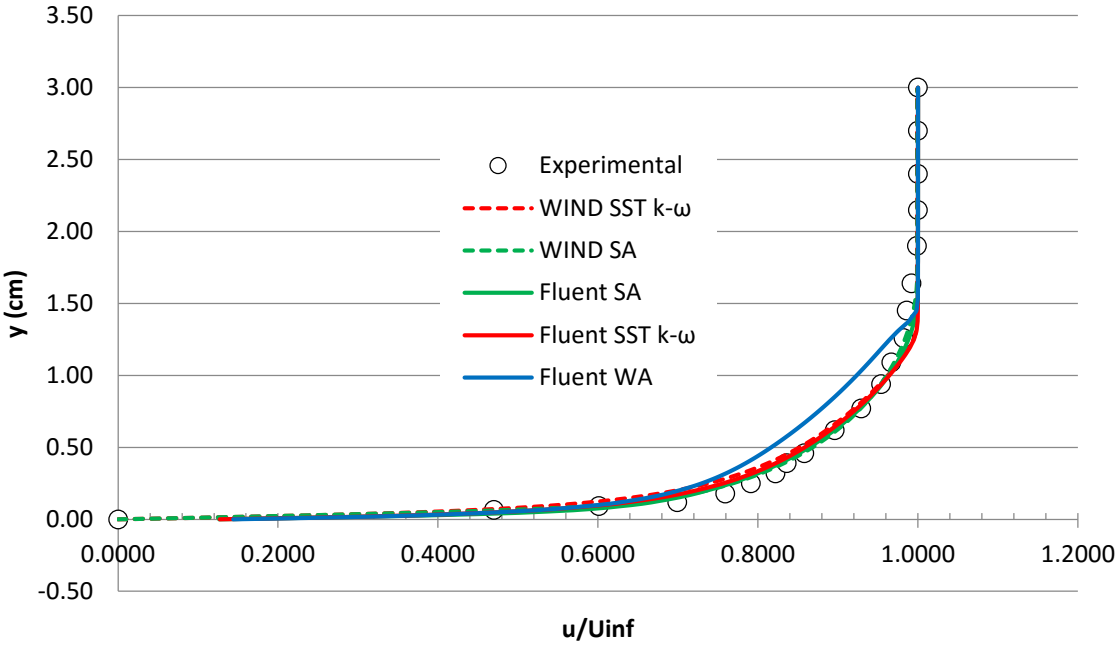

Figure 4.16: Upstream velocity profile at 6.00 cm from partial axisymmetric 20° flare

For the upstream temperature profile, given in Figure 4.17, the WA model is rather accurate in predicting a profile very similar to that of the experiment. As before, little distinction can be made between the results given by the WIND and Fluent SST *k-ω* and SA models. All these models deviate from the experimental and WA results at T/T_{inf} ~ 0.85 to 1.00.

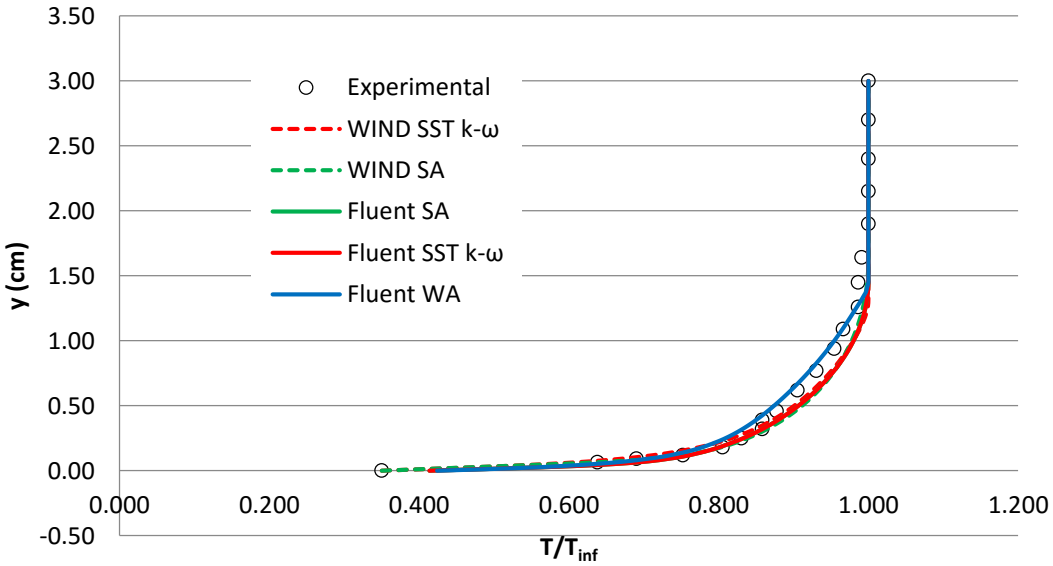

Figure 4.17: Upstream temperature profile at 6.00 cm from 20° flare

The velocity profile at 6.00 cm from the flare is shown in Figure 4.18. All three models underpredict the velocity compared to the experiment. The WA model is the least accurate, followed by the SA and SST *k-ω* models which give similar results. This is most likely due to the fact that all three models predict a thicker boundary layer than what is seen in the experiment.

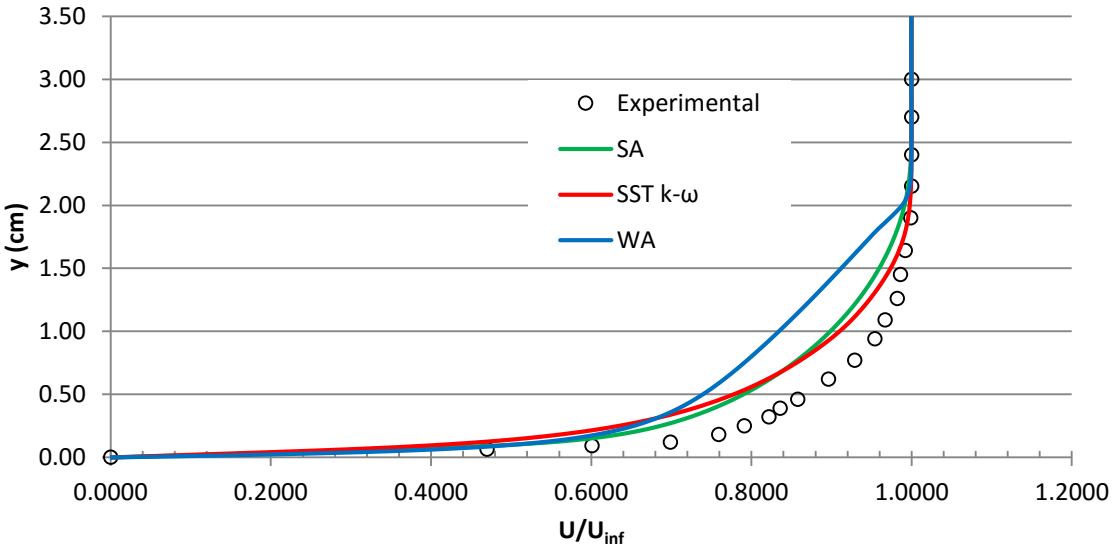

Figure 4.18: Velocity profile for full body axisymmetric flare at x = 6.00 cm from flare.

4.4 Flow due to an Impinging Shock on a Flat Plate

The final case investigated was that of a 2D impinging shock boundary layer interaction for angles, β = 6°, 10°, and 14°. The flow conditions were set to match the experiment by Schulein et al [19]. The freestream boundary conditions were set as follows: Mach number M=*5*; total temperature T_0=*410* K; total pressure P_0=2.12 MPa; and unit Reynolds number Re=40x10^6 m^{-1}. The wall temperature was T_w=300 K. The test model geometry is shown in Figure 4.19.

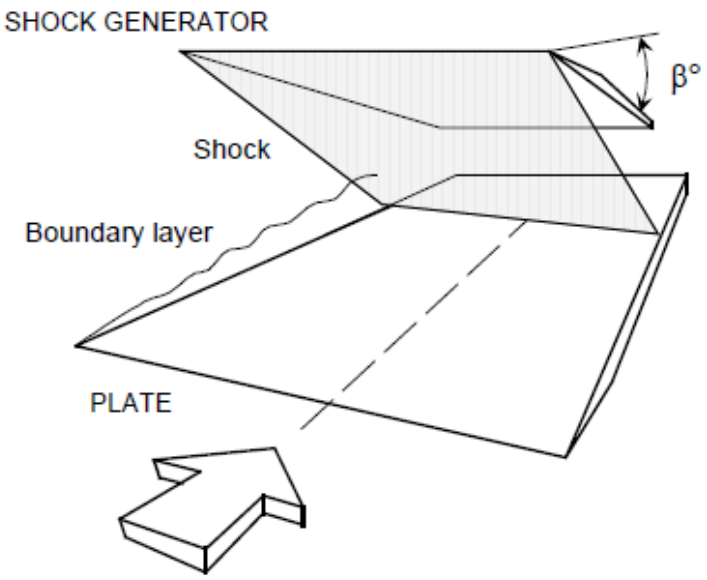

Figure 4.19: Test model geometry for a shock impinging on a flat plate [11]

The original mesh for the impinging shock case has 60000 cells with 60021 nodes. The meshes for the impinging shock cases for β = 6°, 10°, and 14° are shown in Figure 4.20, Figure 4.21, and Figure 4.22 respectively. The mesh for each angle, β, was refined several times, applying the adaption to the gradient of the static pressure. The mesh information is given in Table 4.4.

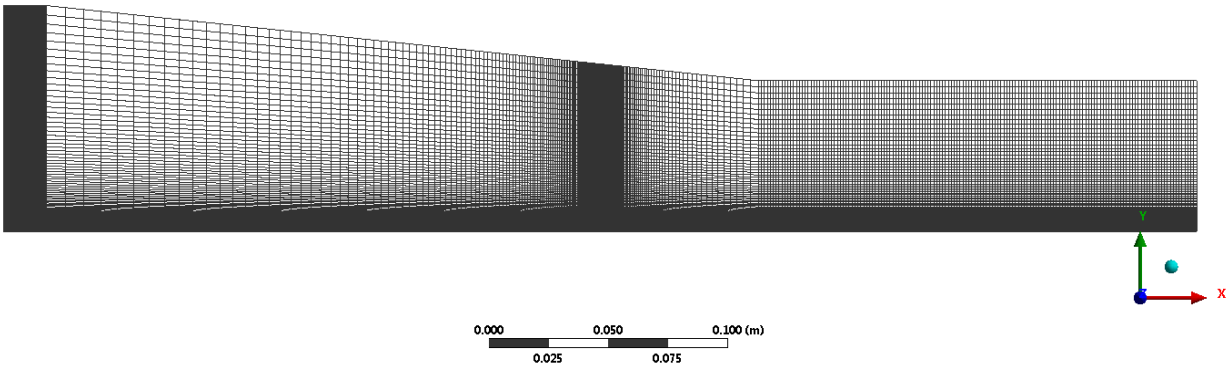

Figure 4.20: Original mesh for impinging shock at β = 6°

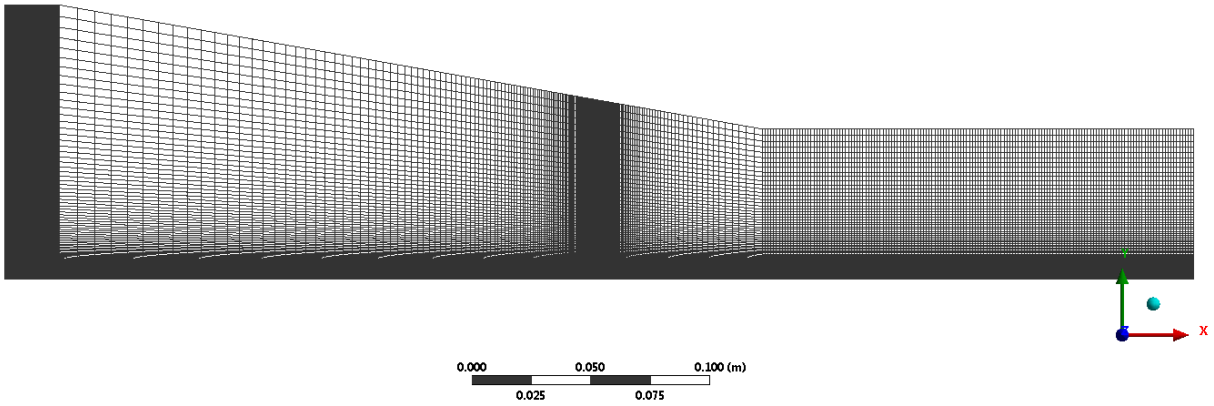

Figure 4.21: Original mesh for impinging shock at β = 10°

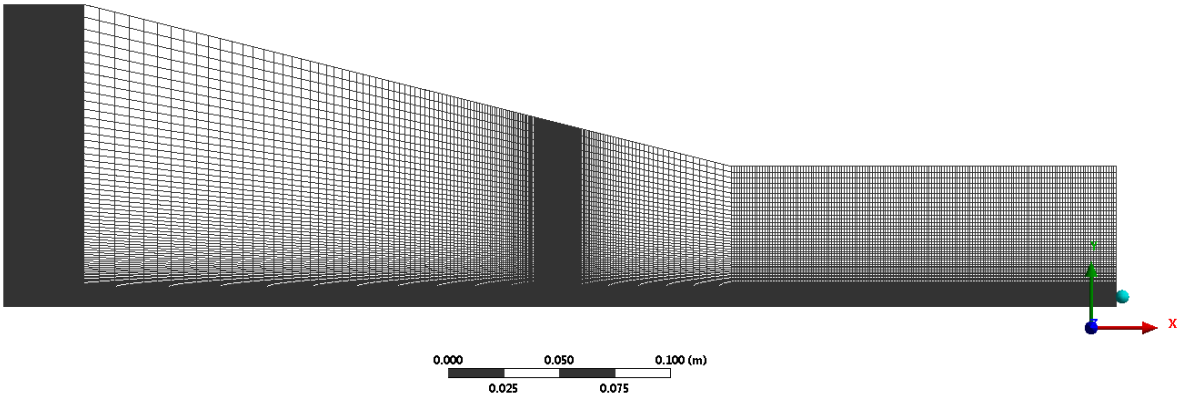

Figure 4.22: Original mesh for impinging shock at β = 14°

Table 4.4: Mesh information for a shock impinging on a flat plate for SA, SST *k-ω* and WA model

β	6°			10°			14°		
Model	SA	SST	WA	SA	SST	WA	SA	SST	WA
Nodes	66587	63635	84006	68383	69544	69637	63285	71392	66786
Cells	65097	62475	81135	66492	67611	67692	62130	69072	65169

The computed P_{wall}/P_{inf} for the β = 6° case is shown in Figure 4.23. The SA and SST *k-ω* models perform relatively well throughout. The WA model underpredicts the surface pressure from x ~ 0.340 to 0.390 m and consequently, it does not match the experimental data as well as the SA and SST *k-ω* models. Leading up to the impinging shock location and downstream of the interaction region, generally good agreement with the experimental data can be seen for all three turbulence models.

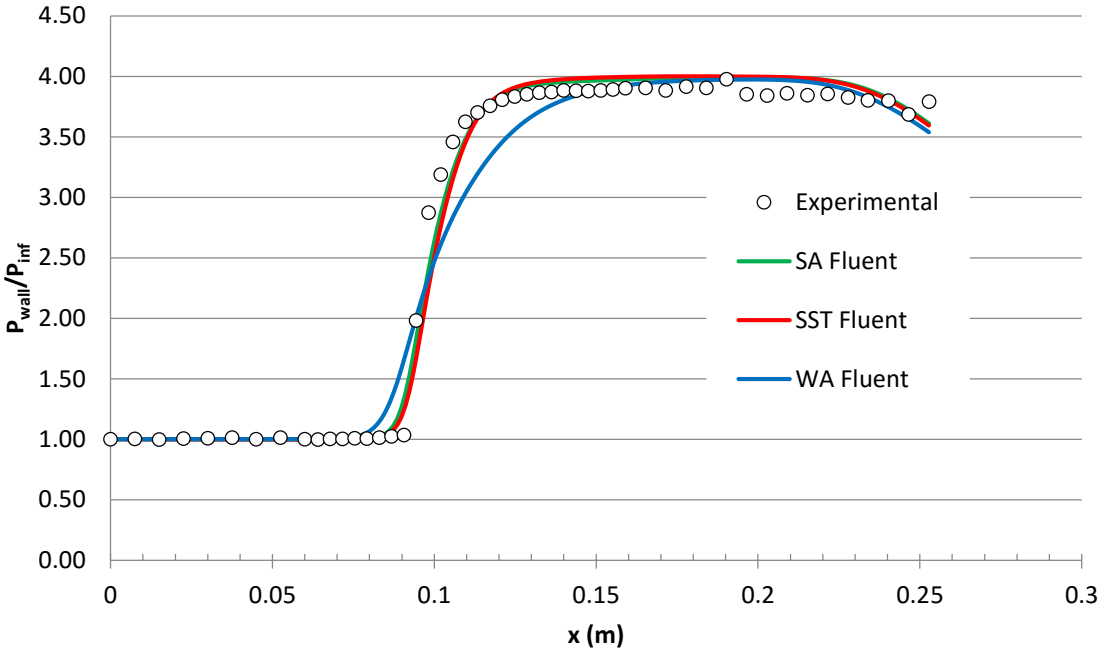

Figure 4.23: P_{wall}/P_{inf} vs. x (m) for β = 6° impinging shock

Looking at the wall pressure for the β = 10° case, the SST *k-ω* model performs the best in matching the results with the experiment. The SST *k-ω* model is the only turbulence model that predicts the flow separation at x ~ 0.330 m. The SA and WA models give nearly identical results until x ~ 0.350 m, where the WA model overpredicts surface pressure.

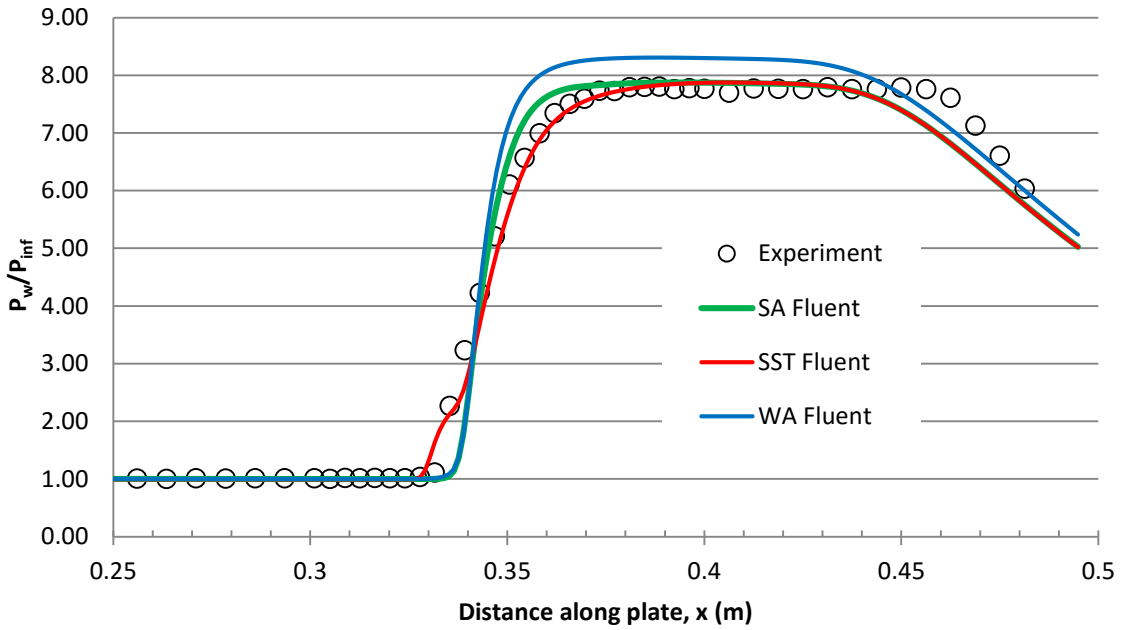

Figure 4.24: Surface pressure for the β = 10° impinging shock

The wall pressure of the $\beta = 14°$ case is given in Figure 4.25. The SST *k*-ω model once more gives the best result in matching the experimental data, capturing the flow separation accurately. The SA model also predicts flow separation, but predicts a much smaller region than that found in the experiment. The WA model fails to predict flow separation. After the shock impingement location, the WA and SA models overpredict the surface pressure, with the WA model showing a larger overprediction than the SA model. The SST *k*-ω model gives the best prediction of the experimental data. Further downstream of the shock, all three models give nearly identical results and follow the experimental trend.

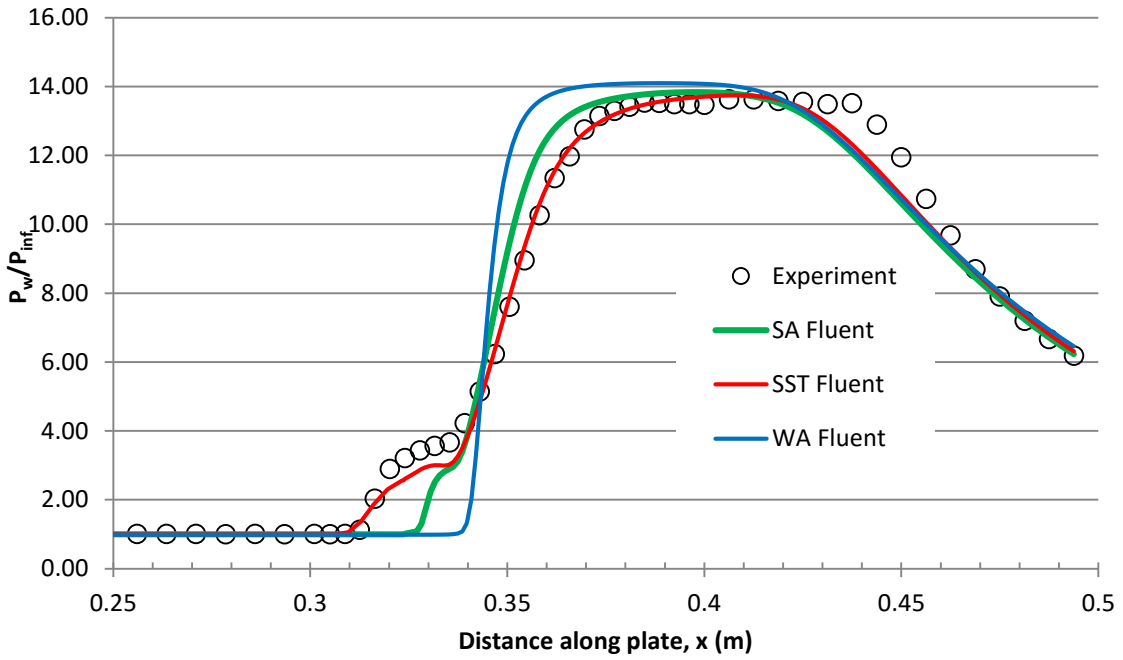

Figure 4.25: Surface pressure for the β = 14° impinging shock

The velocity profile measurements were taken at several positions along the plate at various sections. The sections used for the validation of the turbulence models are sections 7, 8, 9, and 10 in the experiment. Because the geometry of each case varied depending on the impinging shock angle, the positions of the sections differ slightly. The coordinates for sections 7, 8, 9, and 10 are given in Table 4.5.

Table 4.5: Coordinates of the measurement points at various sections for a shock impinging on a flat plate

β	6°		10°		14°	
Coordinate (mm)	x	y	x	y	x	y
7	376	4.5	376	4.1	376	7.1
8	396	5.5	396	6.6	396	5.1
9	426	7.2	426	6.15	426	10.1
10	460	8.1	449	6.35	--	--

Figure 4.26 shows the velocity profiles at four locations along the flat plate for $\beta = 6°$. Generally, all three models perform well in predicting the experimental data. The WA model follows the trend of the experimental data at sections 7, 8, and 9, but because of the prediction of a thicker boundary layer, it predicts smaller values of velocity near the wall than the experiment. The SA and SST *k*-ω models are generally in good agreement at sections 7, 8, and 9, with the SA model outperforming the SST *k*-ω model at section 7. At section 10, all three models give essentially identical results and follow the experimental data satisfactorily.

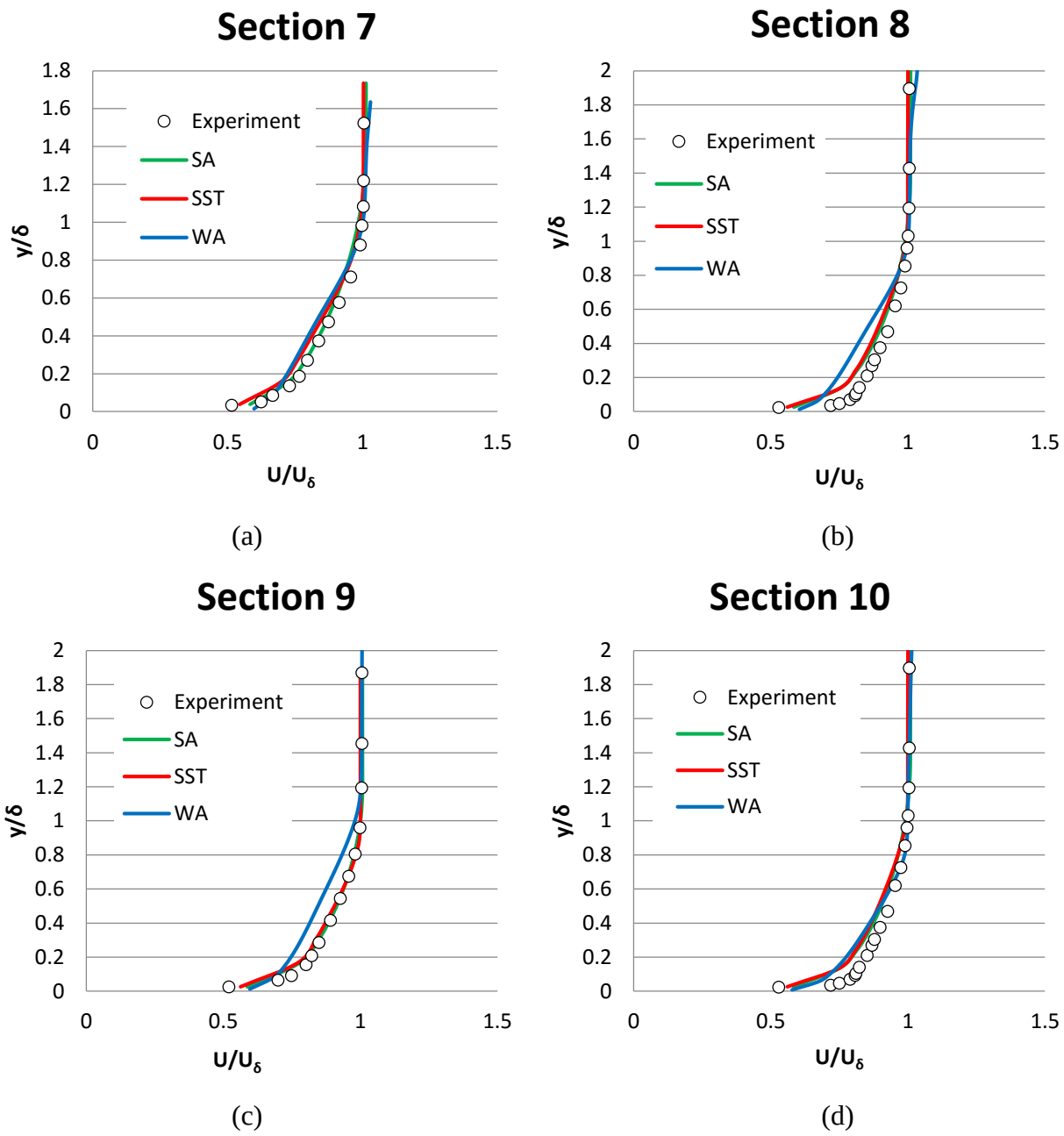

Figure 4.26: Velocity profiles for β = 6° impinging shock case at (a) Section 7, (b) Section 8, (c) Section 9, and (d) Section 10

The velocity profiles for β = 10° in Figure 4.27 show that closer to the shock, the SA model outperforms the WA and SST *k-ω* models. The WA model tends to overpredict the velocity and the SST *k-ω* model underpredicts it. The observed trend in the WA model is expected since for β

= 10° the WA model predicts a thin boundary layer. On the other hand, the SST *k-ω* model predicts the thickest boundary layer. At the section furthest away from the shock location, section 10, all three models are not quite accurate but follow the experimental trend well.

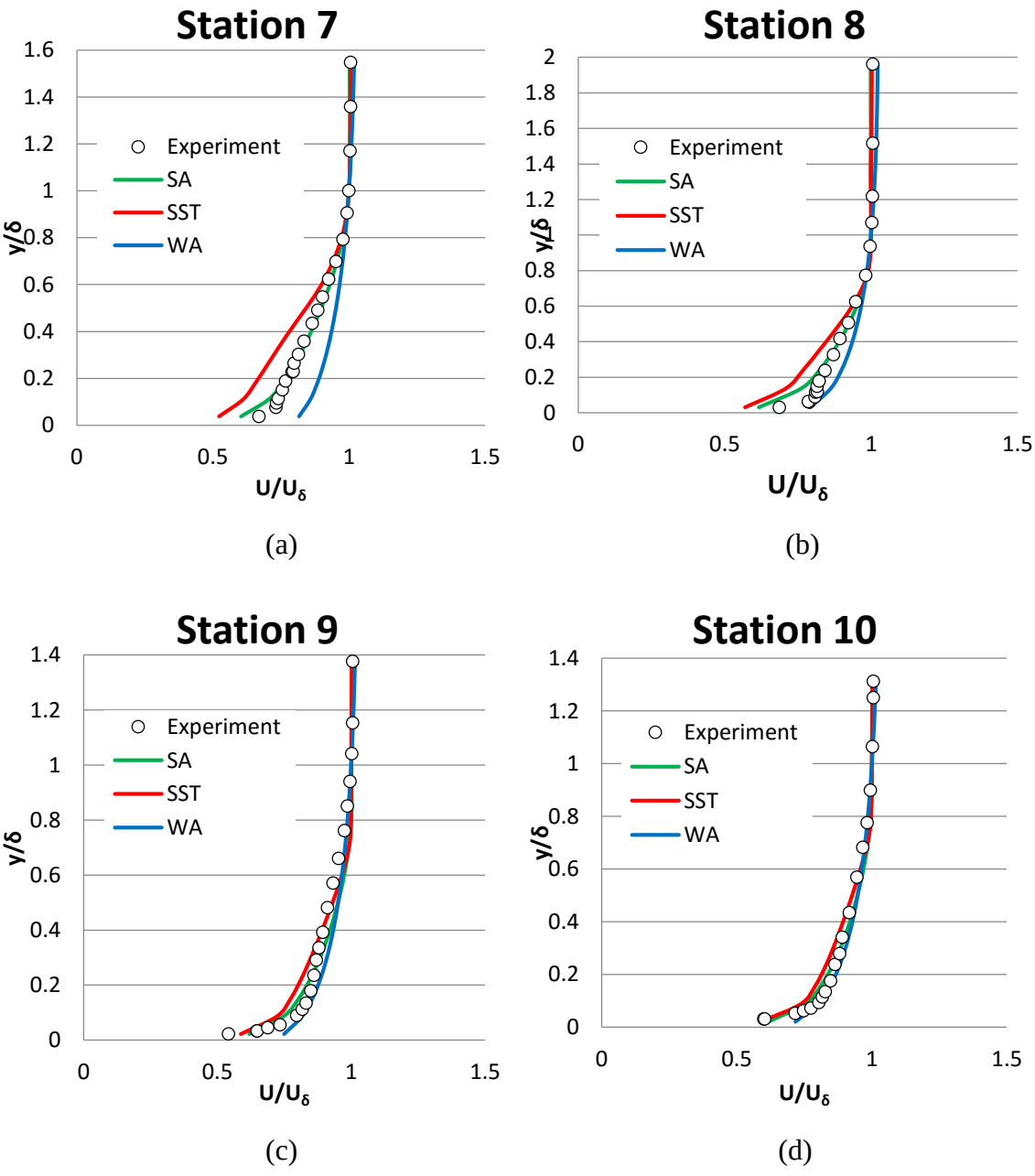

Figure 4.27: Velocity profiles for β = 10° impinging shock case at (a) Section 7, (b) Section 8, (c) Section 9, and (d) Section 10

Finally, we examine the velocity profiles for the β = 14° case in Figure 4.28. Similar to β = 10°, the SA model performs best closest to the shock. The SST *k-ω* model does well in following the trend of the experiment; however, it still underpredicts. At sections 8 and 9, the WA model is most accurate.

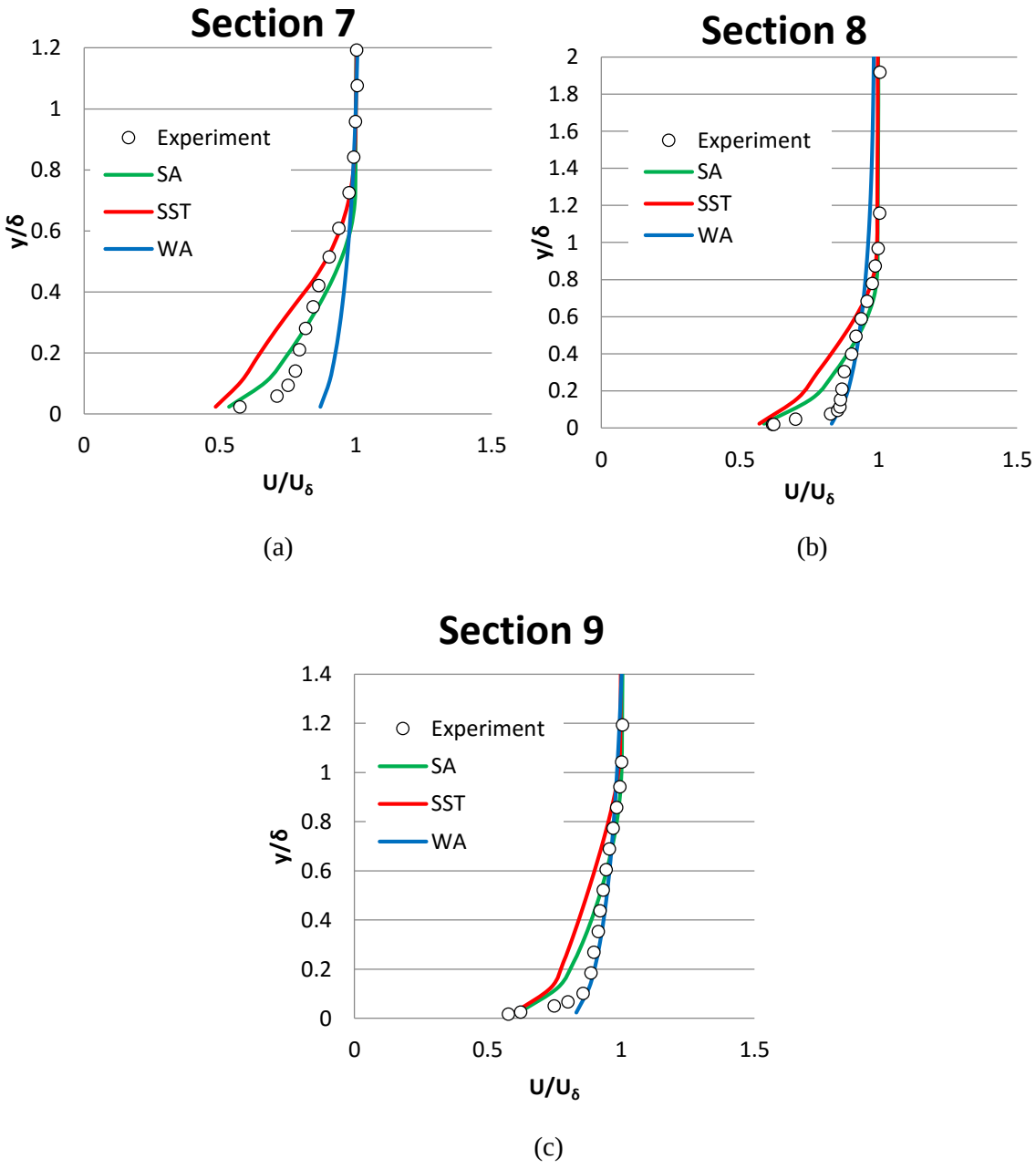

Figure 4.28: Velocity profiles for β = 14° impinging shock case at (a) Section 7, (b) Section 8, and (c) Section 9

Figure 4.29, Figure 4.30, and Figure 4.31, show the Mach number contours for β = 6°, 10° and 14°, respectively.

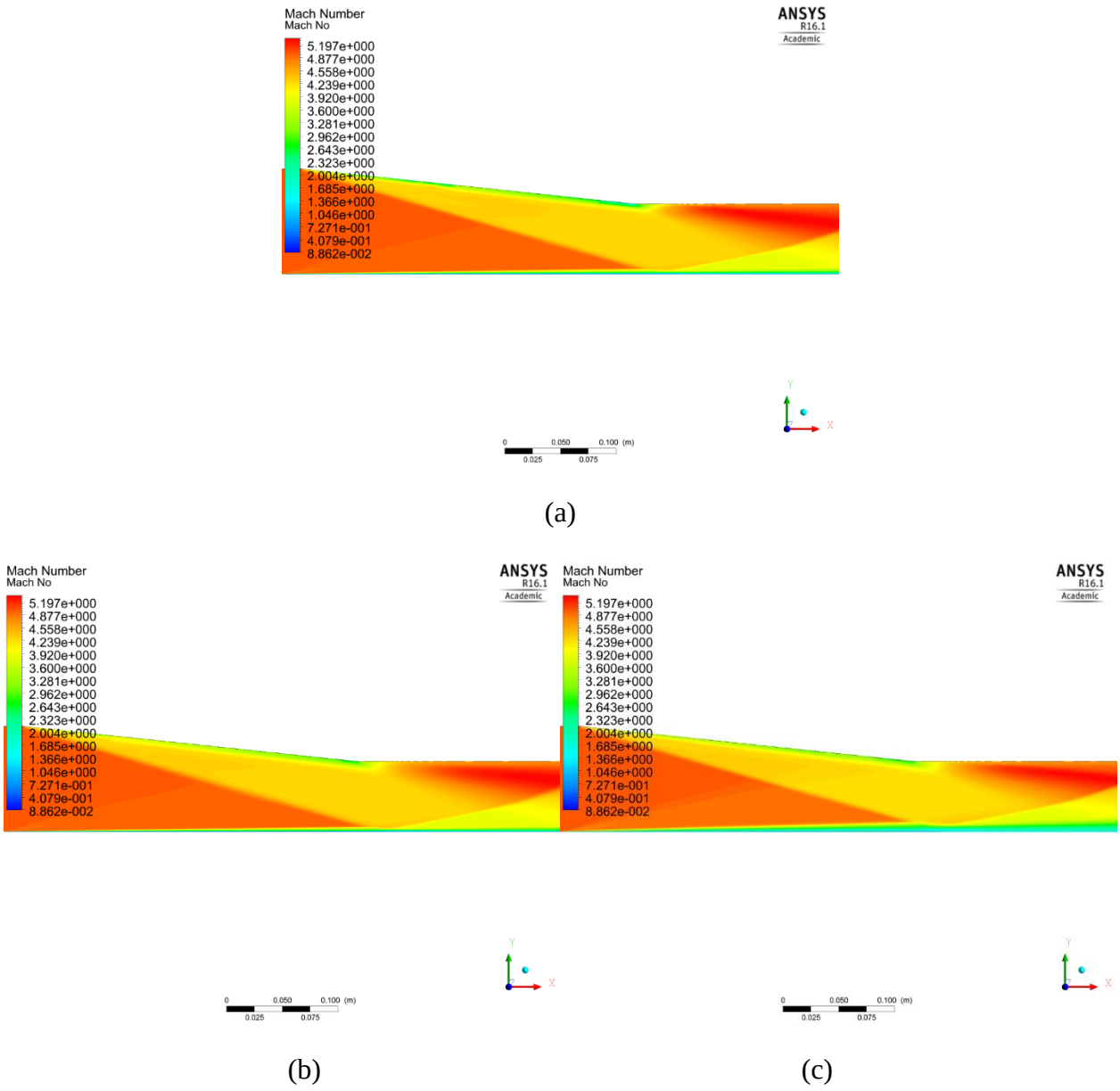

(a)

(b)

(c)

Figure 4.29: Mach number contours for 6° impinging shock case with (a) SA model, (b) SST model and (c) WA model

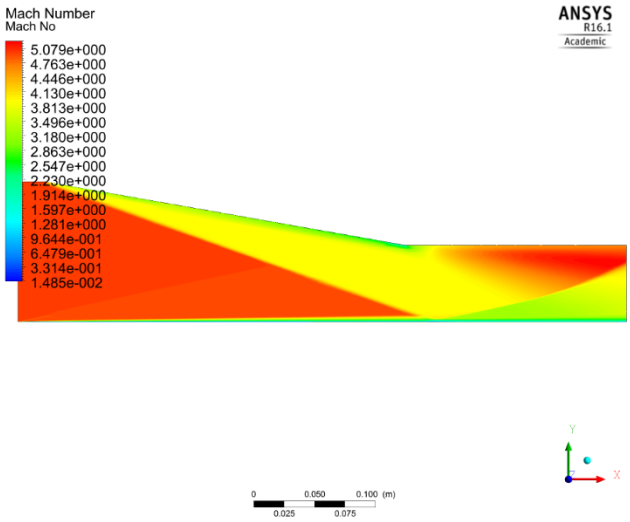

(a)

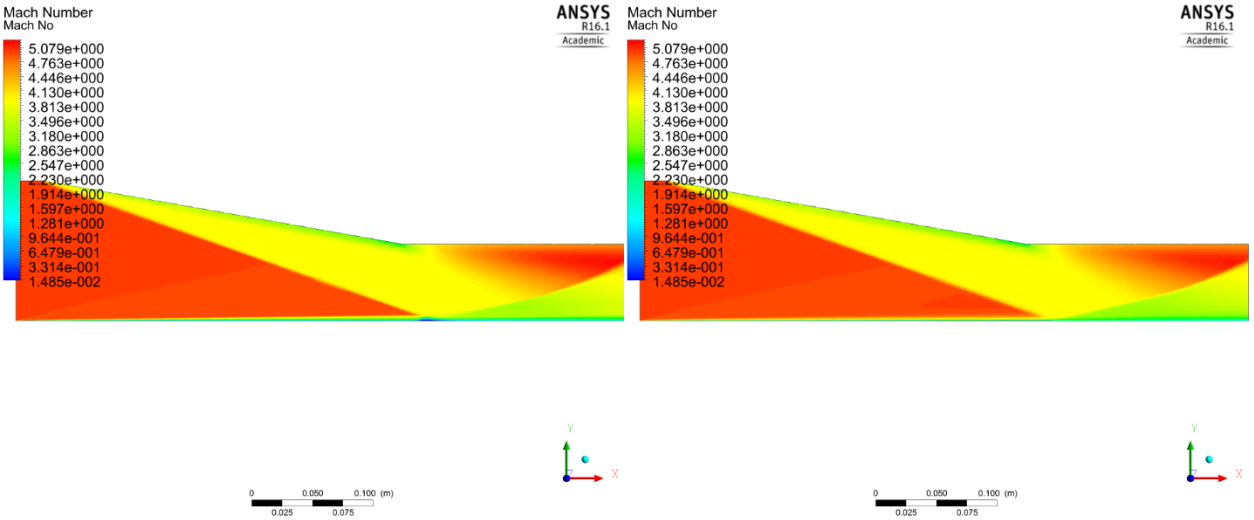

(b) (c)

Figure 4.30: Mach number contours for 10° impinging shock case with (a) SA model, (b) SST model and (c) WA model

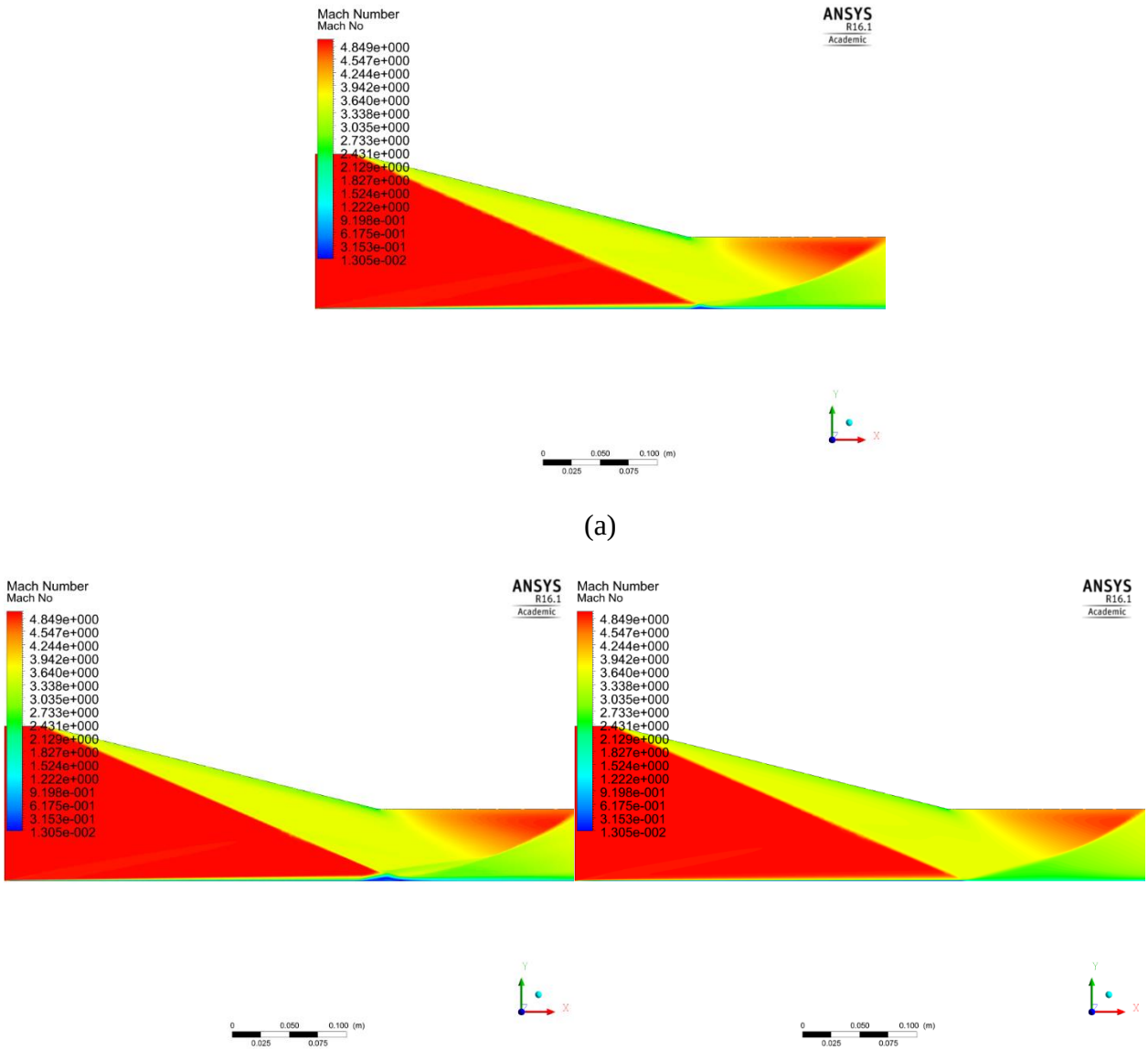

Figure 4.31: Mach number contours for 14° impinging shock case with (a) SA model, (b) SST model and (c) WA model

Chapter 5

Conclusions and Future Research

5.1 Conclusions

In this thesis, three different supersonic flows resulting in shock-wave boundary layer interactions (SWBLI) are simulated using the Reynolds-Averaged Navier-Stokes (RANS) equations in conjunction with three turbulence models—SA, SST k-ω, and WA. The cases include a 2D compression corner, a partial axisymmetric flare, and an impinging shock over a flat plate. The computed results are compared against previously published experimental data. One of the goals of this study was to assess the accuracy of the recently developed WA turbulence model for computing SWBLI flows. For the three cases considered, the WA model was found to be comparable in accuracy to the SA and SST k-ω models.

For the 2D compression corner case, the freestream Mach number was approximately 3. For this case, the three turbulence models satisfactorily predicted the wall pressure profile but failed to adequately predict the skin friction profile. When examining locations upstream of the corner, the WA model performed best at predicting the velocity profiles. The SA and SST k-ω models were generally more accurate downstream of the shock. The WA model correctly predicted the attached flow for the 8° compression corner case, while the SA and SST k-ω models showed some separation that was not observed in the experiment. However, the trend in the computed velocity profiles using the WA model did not agree with the experimental data. For the 16° compression

corner case, all three models predicted flow separation, with the WA model predicting a region of separated flow closer to that found in the experiment.

For the partial axisymmetric flare, the freestream Mach number was approximately 7. In this case, the WA model most accurately predicted the surface wall pressure. The SST *k-ω* incorrectly predicted a large region of flow separation. While the SA model predicted a smaller region of separated flow, it more closely predicted a pressure profile similar to that obtained from the WA model and observed in the experiment. The three turbulence models inaccurately predicted the wall heat transfer but followed the experimental trend.

In the 2D shock impinging on a flat plate case, the freestream Mach number was 5. Impinging shock angles, β, of 6°, 10°, and 14° were simulated. The SA and SST *k-ω* models adequately predicted the wall surface pressure with the SST *k-ω* model giving more accurate predictions. The WA model gave results with trends similar to that of the SA and SST *k-ω* models and the experimental data. The SST *k-ω* model is the only model that predicted flow separation from the impinging shock at $\beta = 10°$. For the $\beta = 14°$ case, the SA model also predicted flow separation, but of a smaller size than that observed in the experiment and predicted by the SST *k-ω* model. The SA model predicted the velocity profiles most accurately. For an impinging shock of $\beta = 14°$, the WA model outperformed the SA and SST *k-ω* models in predicting the velocity profiles.

Comparing the performance of the WA, SA, and SST *k-ω* turbulence models, none of the models could successfully predict all the quantities of interest—namely, the pressure, skin friction, heat transfer and velocity profiles—satisfactorily for all the SWBLI cases considered. However, the three turbulence models successfully followed the trend for these quantities observed in the experimental data with varying degrees of accuracy. This thesis clearly demonstrates the need for

research in the area of turbulence modeling of high-speed compressible SWBLI flow and flows with mild separation bubbles. If accomplished, the development of turbulence models to accurately predict shock-wave boundary layer interactions will lay the foundation for future high-speed aerodynamic capabilities.

5.2 Future Research

Moving forward, research surrounding shock-wave boundary layer interactions (SWBLIs) requires a refinement of the Reynolds Averaged Navier-Stokes (RANS) turbulence models that are currently being employed. Particularly, turbulence models need to possess a multifaceted nature that enables them to systematically solve the various attributes (varying shear layers, flow separation, adverse pressure gradients, etc.) that contribute to the overall flow structure of a SWBLI. Already, turbulence models and flow solvers contain unique functions that further the capabilities of a base turbulence model. For example, ANSYS Fluent applies an extension to the Spalart-Allmaras (SA) model that automatically blends all solution variables from their viscous sublayer to the corresponding logarithmic layer values depending on the dimensionless wall distance variable, y^+ [23]. For SWBLIs, Sinha et al. suggest the addition of a shock-unsteadiness term that will theoretically enable improvements in turbulence prediction [24]. The inclusion of such a term into the turbulence models used in this report may reveal some improvements and is a direction worth investigating.

Lastly, the Wray-Agarwal (WA) turbulence model is in its early stages of development and already it displays a level of accuracy comparable to that of the industry favorites SA and Shear Stress Transport (SST) *k*-ω turbulence models. In order to increase the modeling capabilities of the WA model, additional validations cases need to be conducted. There are several additional SWBLI

cases available through the NASA TMR website that are not investigated in this paper, and in order to reach a further state of confidence with the SA, SST k-ω, and WA models' SWBLI modeling accuracy, the extra cases should be simulated. Depending on the findings, additions and improvements to the base turbulence models can be explored in order to make the turbulence models as true to the experimental data as possible.

References

[1] "History of theoretical fluid dynamics | CWI Amsterdam | Research in mathematics and computer science." [Online]. Available: https://www.cwi.nl/fluiddynamicshistory. [Accessed: 07-Jul-2016].

[2] S. Wolfram, "Historical Notes: Navier-Stokes equations," *WolframScience*. [Online]. Available: https://www.wolframscience.com/reference/notes/996d. [Accessed: 29-Mar-2016].

[3] D. Kuzmin, "Introduction to Computational Fluid Dynamics."

[4] "Two equation turbulence models -- CFD-Wiki, the free CFD reference." [Online]. Available: http://www.cfd-online.com/Wiki/Two_equation_models. [Accessed: 13-Apr-2016].

[5] "NASA's 40% Challenge." [Online]. Available: http://turbmodels.larc.nasa.gov/nasa40percent.html. [Accessed: 07-Jul-2016].

[6] U. A. Force, *X-51A Waverider, U.S. Air Force graphic*. 2010.

[7] A. Ferri, "Experimental Results with Airfoils Tested in the High-speed Tunnel at Guidonia," Jul. 1940.

[8] C. D. Donaldson, "Effects of Interaction Between Normal Shock and Boundary Layer," *NACA 4A27*, 1944.

[9] D. Dolling, "Fifty Years of Shock-Wave/Boundary Layer Interaction Research: What Next?," *AIAA J.*, vol. 39, no. 8, Aug. 2001.

[10] D. W. Holder, H. H. Pearcey, and G. E. Gadd, "The Interaction Between Shock Waves and Boundary Layers," *Br. Aeronaut. Res. Counc. Curr. Pap.*, vol. 180, 1955.

[11] E. Schulein, P. Krogmann, and E. Stanewsky, "Documentation of Two-Dimensional Impinging Shock/Turbulent Boundary Layer Interaction Flow," *DLR Rep.*, vol. DLR IB 223-96 A 49, Oct. 1996.

[12] G. S. Settles, T. J. Fitzpatrick, and S. M. Bogdonoff, "Detailed Study of Attached and Separated Compression Corner Flowfields in High Reynolds Number Supersonic Flow," *AIAA J.*, vol. 17, no. 6, pp. 579–585, 1979.

[13] P. R. Spalart and S. R. Allmaras, “A One Equation Turbulence Model for Aerodynamic Flows,” *AIAA Pap. 1992-0439*, 1992.

[14] F. R. Menter, “Two-Equation Eddy-Viscosity Turbulence Models for Engineering Applications,” *AIAA J.*, vol. 32, no. 8, pp. 1598–1605, Aug. 1994.

[15] “ANSYS Workbench - Wilde Analysis.” [Online]. Available: http://wildeanalysis.co.uk/fea/software/ansys/workbench. [Accessed: 30-Jun-2016].

[16] “Turbulence Modeling Resource.” [Online]. Available: http://turbmodels.larc.nasa.gov/. [Accessed: 09-Jun-2016].

[17] “ANSYS Fluent Users Guide.pdf.” [Online]. Available: http://148.204.81.206/Ansys/150/ANSYS%20Fluent%20Users%20Guide.pdf. [Accessed: 09-Jun-2016].

[18] G. S. Settles and L. J. Dodson, “Supersonic and hypersonic shock/boundary-layer interaction database,” *AIAA J.*, vol. 32, no. 7, pp. 1377–1383, 1994.

[19] K. Muck, E. Spina, and A. Smits, “Compilation of Turbulence Data for an 8 degree Compression Corner at Mach 2.9,” *Tech Rep Rep. MAE-1642 Princet. Univ.*, Apr. 1984.

[20] K. C. Muck, E. Hayakawa, and A. J. Smits, “Compilation of Turbulence Data for a 16 degree Compression Corner at Mach 2.9,” *Tech Rep Rep. MAE-1619 Princet. Univ.*, Nov. 1983.

[21] M. I. Kussoy and C. C. Horstman, “Documentation of Two- and Three-Dimensional Hypersonic Shock Wave/Turbulent Boundary Layer Interaction Flows,” *NASA Tech. Memo. 101075*, Jan. 1989.

[22] Nicholas J. Georgiadis, Christopher L. Rumsey, and George P. Huang, “Revisiting Turbulence Model Validation for High-Mach Number Axisymmetric Compression Corner Flows,” in *53rd AIAA Aerospace Sciences Meeting*, 0 vols., American Institute of Aeronautics and Astronautics, 2015.

[23] “12.2.1. Reynolds Averaged Navier-Stokes (RANS) Turbulence Models.” [Online]. Available: https://www.sharcnet.ca/Software/Ansys/16.2.3/en-us/help/flu_ug/flu_ug_sec_turb_rans.html. [Accessed: 07-Jul-2016].

[24] K. Sinha, K. Mahesh, and G. V. Candler, “Modeling the effect of shock unsteadiness in shock-wave/turbulent boundary layer interactions,” *42nd AIAA Aerosp. Sci. Meet. Exhib.*, no. AIAA 2004 1129, Jan. 2004.

Vita

Francis Kofi Acquaye

Degrees

M.S. Aerospace Engineering
Department of Mechanical Engineering & Materials Science,
Washington University in St Louis, August 2016

B.S. Mechanical Engineering
Department of Mechanical Engineering & Materials Science,
Washington University in St Louis, May 2015

B.A. Physics
Department of Physics,
University of Redlands, May 2015

Publications

Francis Acquaye, Junhui Li, Tim Wray, and Ramesh K. Agarwal. "Validation of the Wray-Agarwal Turbulence Model for Shock-Wave Boundary Layer Interaction Flows", AIAA Paper 2016-3477, 46th AIAA Fluid Dynamics Conference, AIAA 2016 Aviation Forum and Exhibit, Washington DC, 13-17 June 2016.

August 2016